Highlights

MonteCarlo Biphasic Estimation of Fire Properties (McBEF): Part I, Algorithm formulation

Meng Zhou, Arlindo M. da Silva, Jun Wang, David A. Peterson

- A Bayesian biphasic model is developed for sub-pixel fire characterization
- OSSEs assess impacts of phase count, band selection, and temperature variability
- Biphasic and triphasic models improve FRP and heat flux retrievals over mono-phase
- 2.25 μm and day-night bands (DNBs) provide strong constraints on fire phase temperatures
- FRP estimates outperform the empirical method used in standard satellite products

MonteCarlo Biphasic Estimation of Fire Properties (McBEF): Part I, Algorithm formulation

Meng Zhou[a,b], Arlindo M. da Silva[b], Jun Wang[c], David A. Peterson[d]

[a] *Goddard Earth Sciences Technology and Research II, Baltimore, University of Maryland, , Baltimore, 21228, MD, USA*
[b] *Global Modeling and Assimilation Office, NASA Goddard Space Flight Center, , Greenbelt, 20771, MD, USA*
[c] *Department of Chemical and Biochemical Engineering, University of Iowa, , Iowa City, 52242, IA, USA*
[d] *Marine Meteorology Division, Naval Research Laboratory, , Monterey, 93943, CA, USA*

Abstract

Sub-pixel fire characterization is essential for quantifying wildfire energetics, combustion phase dynamics, and their atmospheric impacts from satellite observations. This study presents a series of Observing System Simulation Experiments (OSSEs) to systematically evaluate the influence of temperature phase complexity, channel selection, and intra-phase temperature heterogeneity on the performance of a Bayesian retrieval framework. Using synthetic observations derived from a multi-phase radiance model, we assess retrieval skill across key fire properties—including Fire Radiative Power (FRP), visible energy fraction (VEF), and flaming heat flux—under realistic sensor constraints. Results show that a bi-phasic fire model provides a strong balance between accuracy and observational feasibility, outperforming conventional approaches such as Wooster's FRP regression, particularly in low-intensity fire scenarios. FRP is found to be the most resilient parameter to model and characterize observational uncertainties, while VEF and heat flux estimates are more sensitive to both fire phase partitioning and spectral coverage. Shortwave and mid-infrared bands, especially the day-night band (DNB) and 2.25 μm channels, are shown to offer the greatest constraint on retrieval accuracy. We further analyze the impact of intra-phase temperature variability and propose practical filtering strategies for identifying low-confidence cases, such as smoldering-dominated fires. This paper serves as the first part of a companion study on multi-channel fire retrieval. In the subsequent paper, we apply the bi-phasic Bayesian framework to real VIIRS nighttime observations and assess algorithm performance in an operational setting.

Keywords: Wildfire, sub-pixel characterization, flaming temperature, smoldering temperature, fire radiative power, modified combustion efficiency, heat flux, OSSE, Bayesian, retrievals

---

1. Introduction

Accurate parameterization of wildfires is essential for estimating biomass burning emissions and their vertical injection profiles–two critical inputs for fire weather forecasting and post–impact assessments. This need has become increasingly urgent due to the rising frequency and intensity of wildfires, expanding burned areas, and lengthening fire seasons driven by climate change (Abatzoglou and Williams, 2016; Bondur et al., 2020; Goss et al., 2020; Touma et al., 2022). These trends pose growing threats to public safety and environmental sustainability (Xu et al., 2020; Congressional Budget Office, 2022). Satellite-based remote sensing has become an indispensable tool for near real-time (NRT) wildfire monitoring (Giglio et al., 2016; Wooster et al., 2012; Schmidt, 2020; Csiszar et al., 2014; Schroeder et al., 2014; Polivka et al., 2016; Zhou et al., 2023), supporting fire response strategies, forecasting, and post-fire evaluation (Chuvieco et al., 2020; Giglio et al., 2006). NRT fire detections and characterizations from the MODerate Resolution Imaging Spectroradiometer (MODIS; Giglio et al., 2016) and the Visible Infrared Imaging Radiometer Suite (VIIRS; Schroeder et al., 2014), distributed via platforms such as the Fire Information for Resource Management System (FIRMS; Davies et al., 2008), have been critical to tracking fire evolution, informing firefighting operations, and coordinating evacuations.

Over the past two decades, global spaceborne fire detection products have primarily provided two bulk properties of wildfire: fire location and fire radiative power (FRP; Schroeder et al., 2014; Giglio et al., 2016). Fire locations are identified through a bi-spectral contrast approach, typically using a fire-sensitive mid-wave infrared (MWIR) band near 4 μm and a thermal infrared (TIR) background-sensitive band around 11 μm (Dozier, 1981; Justice et al., 2002; Schroeder et al., 2014; Zhou et al., 2023). The active fire locations are then integrated to estimate burned area (Giglio et al., 2006). FRP, which quantifies the rate of radiative energy emitted by active fires, is typically derived via empirical regression using brightness temperatures or anomalies in MWIR and TIR radiance (Justice et al., 2002; Wooster et al., 2003; Deng et al., 2024). Burned area and FRP serve as key inputs for global and regional fire emission inventories such as the Global Fire Emissions Database (GFED; Van Der Werf et al., 2017), Quick Fire Emissions Dataset (QFED; Darmenov and da Silva, 2015), and the Global Fire Assimilation System (GFAS; Kaiser et al., 2013), which support both NRT air quality forecasts and long-term climate impact studies (Warneke et al., 2023; Pan et al., 2020; Li et al., 2022). In parallel with these bulk estimates, efforts have been made to retrieve sub-pixel fire properties by combining MWIR and TIR observations to estimate a single fire temperature and fractional area. This is typically achieved using the bi-spectral Dozier method (BSDM) (Dozier, 1981) or similar sub-pixel techniques (Menzel et al., 1991; Eckmann et al., 2009). Although BSDM is subject to uncertainties, particularly due to its sensitivity to background temperature estimates and subpixel temperature inhogeneities(Giglio and Kendall, 2001), subsequent studies have shown that such uncertainties can be mitigated with appropriate treatment (Peterson et al., 2013; Peterson and Wang, 2013). Notably, the retrieved temperature and fractional area provide stronger constraints than FRP or total pixel area when estimating smoke injection heights (Peterson et al., 2014).

The availability of multi-channel fire-sensitive observations now allows the extension of Dozier's mono-phasic model to multi-phase models that better capture wildfire heterogeneity. In this study, we extend Dozier's assumption to a bi-phasic model separating flaming and smoldering phases. We develop the Monte Carlo Biphasic Estimation of Fire Properties (McBEF) algorithm, which retrieves phase-specific temperatures and fractional areas from multi-channel observations using a Bayesian inference framework. This paper is the first in a two-part series. Here, we focus on a suite of Observing System Simulation Experiments (OSSEs) designed to investigate the feasibility, behavior, and benefits of using a bi-phasic fire model for sub-pixel characterization. Specifically, we examine the roles of model complexity, channel selection, and intra-phase temperature heterogeneity on retrieval accuracy. In the companion paper (Zhou et al., 2026), we apply the McBEF algorithm to VIIRS nighttime observations and validate its performance using multiple real-world wildfire events.

The remainder of this paper is organized as follows: Section 2 presents the general formulation of the problem, the basis for the generation of synthetic satellite fire observations in section 4. Section 3 introduces the Bayesian estimation framework. Section 4 presents the the specifics the numerical experiment setup and the results of the OSSE-based theoretical analysis. Section 5 presents a summary of key findings.

2. Formulation of the Problem: Remote Sensing of Multi-phasic Fires

In the absence of solar contamination, the signal received from a fire event by a moderate-resolution spaceborne sensor can be modeled using a spectral radiance formulation that accounts for contributions from the fire, background, atmosphere, surface, and sensor characteristics, given by,

$$L(\boldsymbol{\lambda}, T_b) = \int B(T, \boldsymbol{\lambda}) a(T) dT + B(T_b, \boldsymbol{\lambda}) \left(1 - \int a(T) dT\right) \tag{1}$$

Here, T_b represents the background temperature of the surrounding environment and $\boldsymbol{\lambda}$ is the vector of the central wavelength of interest. The function $a(T)$ describes a continuous temperature-area distribution that reflects the sub-pixel variability in fire temperature, influenced by fuel type, load, moisture, topography, and meteorological conditions. The term $B(T, \lambda)$ denotes the top-of-atmosphere (TOA) radiance at temperature T and a given wavelength λ, defined as:

$$B(T, \lambda) = \frac{\int_0^\infty \tau(\lambda)\epsilon(\lambda)P(\lambda, T)\Phi(\lambda)d\lambda}{\int_0^\infty \Phi(\lambda)d\lambda} \tag{2}$$

where $P(\lambda, T)$ is the Planck function, $\Phi(\lambda)$ is the sensor spectral response function, $\tau(\lambda)$ is the atmospheric transmittance, and $\epsilon(\lambda)$ is the emissivity of the emitter. This model assumes the fire behaves as a blackbody or greybody emitter and is valid in spectral regions where fire radiance is predominantly governed by Planckian emission. Narrow alkali metal emission lines (e.g., sodium or potassium), generated by ionization of metallic compounds, are not accounted for in Eq. 1.

In practice, the continuous temperature–area function $a(T)$ cannot be directly retrieved from the limited number of spectral observations available with current satellite sensors. To make the problem tractable, most fire characterization methods approximate the temperature structure using a finite set of temperature phases, each with an associated fractional area. Under this assumption, Eq. 1 can be discretized as:

$$L(\boldsymbol{T}, \boldsymbol{a}, \boldsymbol{\lambda}, T_b) = \sum_i B(T_i, \boldsymbol{\lambda})\, a(T_i) + B(T_b, \boldsymbol{\lambda}) \left(1 - \sum_i a(T_i)\right) \tag{3}$$

Here, $\boldsymbol{T} = \{T_i\}$ and $\boldsymbol{a} = \{a(T_i)\}$ represent the temperatures and fractional areas of the finite temperature phases, respectively. The retrieval problem therefore depends critically on two factors: (1) the number of temperature phases used to represent the sub-pixel fire structure, and (2) the number and spectral placement of observation channels provided by the sensor.

In the finite-phase formulation above, the choice of how many phases to include recovers well-known special cases: a single phase yields the classic monophasic model, two phases the bi-phasic flaming–smoldering model, and three phases extensions that include a cooling/recently burned component. The seminal monophasic fire model proposed by Dozier (1981) assumes a sub-pixel hot source at temperature T_f occupying a fractional area a within a cooler background at temperature T_b. Despite its simplicity, this model established the theoretical foundation for sub-pixel fire characterization and has been widely adopted in satellite fire retrieval algorithms (e.g., Peterson et al., 2013; Peterson and Wang, 2013). To represent more realistic combustion conditions, Kaufman et al. (1998) introduced a bi-phasic framework that separately characterizes flaming and smoldering components, while Wooster et al. (2003) extended this approach by adding a cooling phase to account for recently burned areas in spatially extensive fire scenes. These multi-phase representations, though conceptually more complete, have been used primarily for empirical calibration and cross-sensor algorithm development due to the limited number of available thermal channels. Early satellite instruments such as AVHRR provided only two suitable bands near 4 μm and 11 μm, constraining retrievals to bi-spectral formulations (Li et al., 2001; Dozier, 1981). The inclusion of additional shortwave and midwave infrared channels in later sensors such as MODIS, VIIRS, and SLSTR has since enabled a more comprehensive representation of sub-pixel combustion processes, motivating the development of physically based multi-phase retrieval frameworks as described in Section 3.

3. Retrieval of Fire Properties from Multi-wavelength Sensors

With the forward model established (Section 2) and the historical context summarized above, we focus here on retrieval. We first present the BSDM formulation as a notational baseline (Section 3.1), then extend to a bi-phasic forward model (Section 3.2) and a Bayesian inference framework (McBEF) to address nonlinearity and temperature–area trade-offs in multi-channel data.

3.1. Dozier's Algorithm for Uni-phasic Fires

Under the uni-phasic assumption, the classic BSDM treated the at-sensor radiance at 4 μm and 11 μm as a linear mixture of a hot sub-pixel component with temperature T_f and fractional area a, and a background at temperature T_b:

$$L_4 = aB_4(T_f) + (1 - a)B_4(T_B) \tag{4}$$

$$L_{11} = aB_{11}(T_f) + (1 - a)B_{11}(T_B) \tag{5}$$

Here, B_4 and B_{11} are the TOA radiance operators at 4 μm and 11 μm. Given observed radiances L_4, L_{11}, and an estimate of T_B (e.g., from non-fire neighbors or longwave measurements), Eq. (4) can be solved using optimal estimation taking in consideration the observational uncertainties and (T_f, a) as control variables. However, the classic BSDM takes the simplistic view of treating this as a simple case of two equations in the two unknowns (T_f, a). Eliminating a yields a single implicit nonlinear equation for T_f:

$$a = \frac{L_4 - B_4(T_B)}{B_4(T_f) - B_4(T_B)} = \frac{L_{11} - B_{11}(T_b)}{B_{11}(T_f) - B_{11}(T_b)}, \tag{6}$$

which is solved numerically; the common ratio gives a. Despite its simplicity, this formulation established the foundation for sub-pixel fire retrieval and has been widely adopted and adapted in satellite algorithms (e.g., Giglio and Kendall, 2001; Peterson et al., 2013; Peterson and Wang, 2013). Notice that (Giglio and Kendall, 2001) questions the validity of Dozier's approach for heterogenous fires.

3.2. Generalization to Bi-phasic Fires

To better represent heterogenous fire pixels, the next simple model allows for separate (flaming, smoldering) phases with temperatures (T_f, T_s) and fractional areas (a_f, a_s):

$$L_k \;=\; a_f\, B_k(T_f) \;+\; a_s\, B_k(T_s) \;+\; \big(1 - a_f - a_s\big)\, B_k(T_b), \qquad k = 1, \ldots, K, \tag{7}$$

with constraints $a_f \geq 0$, $a_s \geq 0$, and $a_f + a_s \leq 1$. Even with known T_b, the unknown parameter vector $\boldsymbol{\theta} = (T_f, T_s, a_f, a_s)$ is four-dimensional; hence, a purely deterministic solution requires at least $K \geq 4$ informative channels and remains sensitive to measurement noise and forward-model mismatch. In practice (and as quantified later in Fig. 7), information content varies strongly with wavelength. Shortwave/visible and midwave channels, such as VIIRS DNB (0.7∼0.9μm), 1.24 μm, 1.60 μm, and 2.25 μm, tend to have higher leverage on the flaming temperature T_f and its fractional area because of the large brightness contrast with the background. By contrast, longwave thermal channels (e.g., 8.55, 10.5, and 12.01 μm) better anchor the cooler components (stabilizing T_b and improving sensitivity to T_s). As additional bands are incorporated, the feasible region in (T_f, T_s) progressively contracts and the temperature–area degeneracy relaxes, leading to a sharper joint likelihood. This motivates a probabilistic treatment that can coherently fuse channels with heterogeneous sensitivity and noise. We revisit these effects quantitatively in Section 4 (Fig. 7), where we compare single-band and multi-band configurations within an OSSE using VIIRS-like SNR.

3.3. Bayesian Retrieval Formulation for Multi-phasic Fires

The characterization of wildfires can be framed as a parametric estimation problem that involves determining a set of parameters $\boldsymbol{\theta}$ from a set of observed data $\boldsymbol{y}$, given inputs $\boldsymbol{x}$ in a noises system. The starting point is the *measurement equation*,

$$\boldsymbol{y} = f(\boldsymbol{x}; \boldsymbol{\theta}) + \boldsymbol{\epsilon}^o \tag{8}$$

where the forward operator f maps the input $\boldsymbol{x}$ to the observable $\boldsymbol{y}$; $\boldsymbol{\epsilon}^o$ represents the observation error that accounts for errors in the forward model f, detector noise and error of representativeness (Rodgers, 1990). As it is common practice, here we assume that $\boldsymbol{\epsilon}^o$ follows a known probability distribution (e.g., Gaussian). For our specific problem, f is the band radiance model that simulates the radiance emitted by wildfires at selected wavelengths. This model is constructed by making specific assumptions about the number of fire phases (flaming, smoldering, cooling, etc), accounting for the sub-pixel temperatures and fractional areas; details will be given in Section 4.1.2.

With prior knowledge of the probability distribution of the parameters $p(\boldsymbol{\theta})$, Bayes's theorem can be used to update this knowledge in light of observed data $\boldsymbol{y}$. The results are posterior distribution of the parameters $\boldsymbol{\theta}$ is given by:

$$p(\boldsymbol{\theta}|\boldsymbol{y},\boldsymbol{x}) = \frac{p(\boldsymbol{y}|\boldsymbol{x};\boldsymbol{\theta})p(\boldsymbol{\theta})}{p(\boldsymbol{x}|\boldsymbol{y})} \tag{9}$$

where $p(\boldsymbol{y}|\boldsymbol{x};\boldsymbol{\theta})$ is the likelihood function which can be obtained from Eqn. 8 under appropriate assumptions about the observation error distribution. $p(\boldsymbol{y}|\boldsymbol{x})$ is the marginal likelihood representing the probability of observing $\boldsymbol{y}$ given $\boldsymbol{x}$ across all theoretical scenarios supported by the prior. Calculating the exact marginal likelihood can be challenging; however $p(\boldsymbol{y}|\boldsymbol{x})$ serves as a normalizing constant to ensure that the posterior distribution $p(\boldsymbol{\theta}|\boldsymbol{y},\boldsymbol{x})$ integrates to one, ensuring it as a proper probability distribution. While further assumptions could be introduced to reduce this to a classic optimal estimation retrieval, the non-gaussianity of the parameters involved calls for a more general application of Bayes' theorem as we will see later. Therefore, we explore the application of Markov Chain Monte Carlo (MCMC, Robert and Casella, 2011) methods for estimating fire properties from multi-wavelength satellite data.

The MCMC algorithm adopted here belongs to a broad class of algorithms used in statistical physics, economics, and computational biology, among other fields, for sampling from complex probability distributions (Gelman et al., 1995). MCMC is particularly useful when direct sampling is difficult due to the high dimensionality of the space or complexity of the distribution. MCMC operates by generating a Markov chain that achieves equilibrium at the desired posterior distribution $p(x)$. This allows the chain to systematically explore the parameter space, with the frequency of visiting any particular region being proportional to the posterior probability of that region. Once the the chain reaches its stationary distribution, samples from the chain can be used as samples from the posterior distribution p to perform Monte Carlo integration for parameter estimation and uncertainty quantification. The MCMC has been sucessfully used on a number atmospheric, oceanic and hydrological applications (e.g., Posselt, 2013; Norris and Silva, 2016, and references within).

Before presenting the details of our MCMC implementation we start describing the Observing System Simulation Experiment (OSSE) framework that will be used to assess the merits of the algorithm.

4. Observing System Simulation Experiments

An Observing System Simulation Experiment (OSSE) is a cost-effective and widely adopted approach for evaluating the potential of a proposed observational systems and data types to advance scientific understanding and prediction capabilities before real-world deployment. OSSEs provide a controlled and flexible testbed for assessing information content, guiding algorithm development, and quantifying uncertainties under well-defined, controlled conditions.

In the context of satellite-based sub-pixel fire characterization, the core challenge lies in approximating the continuous temperature–area distribution $a(T)$ of wildfire scenes using finite-phase fire models such as Eqn. 4 or 7. This approximation is constrained by the limited number of spectral radiance observations available from satellite sensors and the structure of the parametric model used in the estimation. Consequently, two factors primarily govern the quality of retrievals: (1) the number of temperature phases assumed in the fire model, and (2) the number and nature of the spectral channels used in the estimation. These two factors are often interdependent in practice. While increasing the number of phases may improve representation of the fire's thermal heterogeneity, the limited number of spectral radiances and/or the lack of information content in the available channels may render these parameters non-identifiable. Therefore, when designing a fire model to generate a *nature run* able to characterize the strengths and limitations of the algorithm one needs to strike a balance between the generality of the *nature model* (typically more complex than what is assumed by the retrieval) and its complexity (so that a meaning retrieval can still be achieved).

The utility of each spectral channel depends on its inherent information content. For instance, visible bands offer little sensitivity to smoldering temperatures below approximately 600 K, while long-wave infrared channels typically show a weak radiance response to biomass burning conditions. Additionally, the availability of useful observations is inherently limited by sensor design and saturation, environmental constraints, such as solar contamination, surface background interference, and atmospheric absorption, which may render certain wavelengths unusable.

In this section, we design OSSEs to systematically examine the combined effects of fire model complexity and observational channel availability on subpixel fire characterization. We address the following fundamental questions:

- **Assess how the number of temperature phases influences ra-**

diative closure, i.e., the ability of a finite-phase fire model assumed in the retrievalto reconstruct the simulated spectral radiance observations with a more complex fire model;

- **Evaluate the information content of operational channels** and identify the role of each band in constraining sub-pixel fire properties;
- **Investigate the impact of intra-phase temperature heterogeneity** on retrieval accuracy and stability under representative multi-band configurations from current satellite fire monitoring systems.

We begin by describing the overall OSSE configuration and nature run generation, then proceed to address each of these questions in detail in the subsequent subsections.

4.1. OSSE setup

4.1.1. Nature Run

A nature run is a model simulation used to simulate the *ground truth* observations. We used the finite-phase fire model defined in Eqn. 3 to simulate TOA fire radiance. Up to three fire temperature phases are assumed: flaming, smoldering, and residual—plus a homogeneous background are considered. The temperature and corresponding fractional area for each phase were randomly sampled from predefined uniform distributions (Table 1). To represent intra-phase temperature sub-pixel variability, we included both homogeneous and heterogeneous scenarios. The homogeneous model, though simple, is consistent with prior studies (Kaufman et al., 1998; Wooster et al., 2003) and serves as the baseline configuration for phase modeling in our OSSEs; the fire model assumed in the retrievals are homogeneous. In this case, each phase is represented by a single temperature and corresponding fractional area sampled based on Table 1.

Heterogeneous model. For more realistic heterogeneous scenarios (which will allow evaluation the impact of the homogeneous assumption in the retrievals) we adopt a sub-column approach as in Norris and da Silva (2016), in which each phase is represented by an ensemble of sub-phase temperatures. An illustration of this sampling strategy is shown in Fig. A.12. First, a central temperature is prescribed for each phase (green bar), which serves as the midpoint of a predefined intra-phase temperature variation. Based on this

Table 1: Configurations of OSSE fire phase

Phase	Temperature[1]	Fractional area
Flaming	$T_f \sim U(900, 1400)$	$\log\ a_f \sim U(-6, -2)$
Smoldering	$T_s \sim U(460, 900)$	$\log\ a_s \sim U(-5, -1)$
Residual	$T_r \sim U(320, 460)$	$\log\ a_r \sim U(-5, -1)$
Background	$T_b \sim U(295, 25)$	$1 - a_f - a_s - a_r$

[1] Temperature range for different phase are adopted from Rein (2016) and Ward (2001).

central value and the specified temperature heterogeneity, an allowable sampling range is constructed for each phase. Sub-phase temperature members are then sampled uniformly from this range (gray bar). For example, with a heterogeneity of 200 K and a central flaming temperature of 1116 K, the allowed sampling range spans from 1016 K to 1216 K. The fractional area of each phase is evenly divided among its sub-phase members, and the total radiance is computed by summing the contributions from each.

To avoid overlapping between adjacent phases, preventing smoldering sub-phase temperatures from falling within the flaming phase range, we adjust the predefined temperature distributions according to the specified heterogeneity. Specifically, the lower bound is increased by half the temperature variation ($T_l^{\text{new}} = T_l + \Delta T/2$), and the upper bound is decreased by the same amount ($T_u^{\text{new}} = T_u - \Delta T/2$), where ΔT represents the designed intra-phase temperature heterogeneity. For instance, with a heterogeneity of 200 K, the adjusted flaming temperature distribution becomes $U(1000, 1300)$. This adjustment allows full coverage of the designed intra-phase temperature variability while maintaining clear separation between fire phases. Notice that this level of control would be very difficult had we used gaussian distributions for these parameters.

Spectral Coverage. To simulate multi-channel observations we assume that fires are blackbody emitters (emissivity $\epsilon(\lambda) = 1$) across the relevant wavelengths, consistent with common assumptions about fire emissivity. We consider two basic sets of simulations:

Idealized hyper-spectral sensor. As a first step, we consider a uniform hyper-spectral sensor (USS) with wavelengths from 0.5 μm to 12 μm in 0.1 μm steps. Line-by-line radiances are calculated directly from the corresponding Planck function without applying a Relative Sensor Response (RSR) function, thereby reducing complexity. We also neglect atmospheric absorption for this idealized simulation as our primary goal is to disentangle the coupling effects of temperature-phase count and channel selection on fire characterization.

Realistic multi-spectral sensor. For a more realistic multi-channel simulation, we adopt the VIIRS spectral configuration, given that VIIRS is currently one of the most advanced spaceborne fire sensors used operationally. The VIIRS RSR, $\Phi(\lambda)$, is obtained from the NOAA Center for Satellite Applications and Research (`https://ncc.nesdis.noaa.gov/VIIRS/VIIRSSpectralResponseFunctions.php`). We used the the Unified Linearized Vector Radiative Transfer Model (UNL-VRTM, Wang et al., 2020b), specifically developed for wildfire studies, to simulate atmospheric transmittance $\tau(\lambda)$ across the wavelengths of interest. As a first-order approximation, only Rayleigh scattering at standard atmospheric pressure and gas absorption (HITRAN, Rothman et al., 2013) are included. Although aerosols such as smoke could further attenuate fire light via scattering and absorption, these complex effects are excluded from the OSSE for simplicity.

Example Simulation. For illustration, Fig. 1 shows simulated hyper-spectral TOA radiances from various sources that contribute to the fire signal, based on the band radiance model in Eqn. 3. Two homogeneous fire scenarios are presented: 1) one with a flaming component at 1116 K occupying 0.05% of the pixel and a smoldering component at 643 K occupying 0.22%, and 2) another with 1,116 K flaming temperature occupying 0.07% and 642 K smoldering temperature at 0.02%. Assuming a 750 m resolution pixel, the derived FRPs are 35.3 MW and 35.7 MW, representing median to small sized fires. The TOA and surface boundary conditions are given by the zero-air-mass solar spectral irradiance from the American Society for Testing and Materials (ASTM E-490, ASTM, 2000), and a dry grassland spectrum (`splib07a_Grass_dry.5+.5green_AMX28_BECKa_AREF`) from the U.S. Geological Survey (USGS) Spectral Library Version 7 (Kokaly et al., 2017). As shown in Fig. 1, for these fire scenarios, the classic detection and FRP estimation bands (e.g., 3.7∼4.0 μm) primarily capture fire light and terrestrial radiation, with fire light accounting for up to 95% of the signal. At

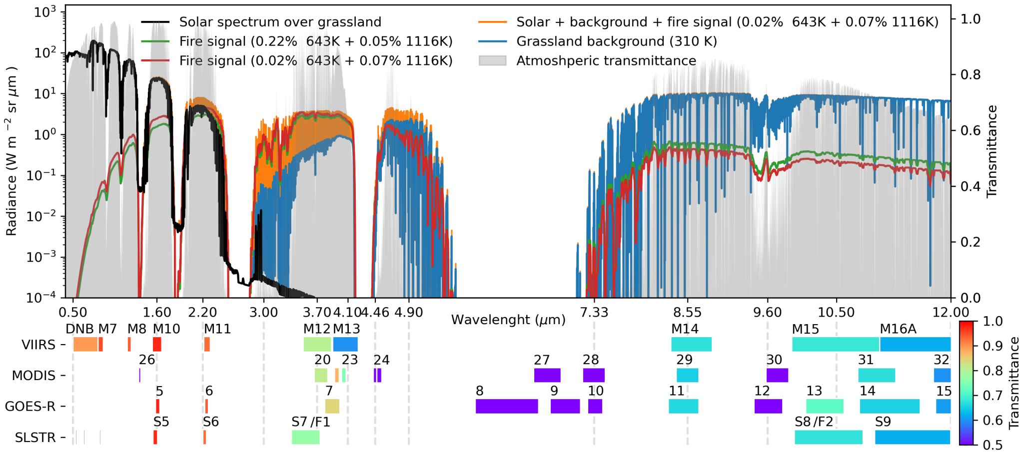

Figure 1: Simulated top of atmosphere (TOA) spectral radiance from visible to thermal infrared (nadir view). The black line is the TOA solar radiance reflected by a grass land surface. The blue line is the radiance emitted by the grassland assuming a temperature of 310 K. The green (smoldering)and red (flaming) line are the spectrum radiance of two bi-phasic fires, respectively. The fire radiance is convoluted to 25 nm spectral resolution for graph clarity. The orange line is the fire and background signal on top of the reflected sunlight. The gray shaded area is the atmosphere transmittance considering gas and Rayleigh scattering. The bottom block plots are the band availability, for both day and night, of VIIRS, MODIS, GOES-R, and SLSTR, color-coded with the corresponding band-wised atmosphere transmittance.

longer wavelengths, terrestrial radiation gradually dominates, though fire signatures can still increase the total signal by approximately 10%. Conversely, at wavelengths below 3 μm, terrestrial radiation has a smaller influence (for a typical Earth surface temperature of 288 K, the background radiance at these shorter wavelengths is below 0.03 W m^{-2} sr^{-1} μm^{-1}). In this range, reflected sunlight and direct upwelling fire light become the main sources of radiance in fire observations. At visible wavelengths, sunlight is four to six orders of magnitude stronger than fire light, so visible data are mostly used for nighttime fire detection and characterization. However, slightly longer wavelengths (around 2.2 μm) reveal more discernible fire signals. For instance, in the simulated flaming-dominated scenario, fire accounts for about 60% of the TOA radiance; in the smoldering scenario, it contributes roughly 15%. This highlights the potential for using 2.2 μm observations to characterize fires both day and night, provided an effective criterion is applied to separate fire emissions from solar contamination.

The lower panel of Fig. 1 summarizes the diurnal band availability and atmospheric transmittance of several widely used spaceborne pyrometers. As shown, beyond the standard 4 μm and 11 μm channels of MODIS, newer radiometers such as VIIRS, SLSTR, and GOES-R ABI include atmospheric window channels at 1.6 μm and 2.25 μm for both daytime and nighttime observations. VIIRS further extends coverage to around 1.24 μm and offers a shorter visible DNB band. These expanded options provide greater flexibility in identifying optimal channel combinations for sub-pixel fire characterization. We summarize the specific combinations used in our OSSEs as follows:

Threshold (Threshold Observation): 4.05 μm (M13), 8.55 μm (M14), 10.5 μm (M15), and 12.01 μm (M16). This configuration includes the same channels used in the classic bi-spectral Dozier method (BSDM) and serves as the reference for our OSSEs.

Best-NGT (Best Nighttime Observation of VIIRS): 0.5∼0.9 μm (DNB), 1.24 μm (M08), 1.6 μm (M10), 2.25 μm (M11), and the Threshold channels. This combination represents the best-case nighttime configuration currently available on VIIRS.

VIIRS-NGT (Common Nighttime Observation of VIIRS): 0.5∼0.9 μm (DNB), 2.25 μm (M11), and the Threshold channels. This represents the most typical nighttime scenario of VIIRS, given that significant data loss in M08 and M10 often limits their availability.

SLSTR-NGT (Best Nighttime Observation of SLSTR and ABI): 1.6 μm (M10), 2.25 μm (M11), and the Threshold channels. This setup reflects a nighttime scenario of SLSTR and ABI.

VIIRS-Day (Possible Daytime Observation for VIIRS, SLSTR, and ABI): 2.25 μm (M11) and the Threshold channels, assuming solar interference in M11 can be effectively mitigated.

A summary configurations and and corresponding objectives is provided in Table 2.

Table 2: Experimental Objectives

Objective	**Fire Phase**	**Bands**	**Heterogeneity**	**Retrieval Model**
Exp 1: Assess how the number of temperature phases influences radiative closure.	Tri-phasic	USS	100 K	Mono-phasic Bi-phasic Tri-phasic
Exp 2: Evaluate the information content of operational channels.	Bi-phasic	Threshold with DNB with 1.24 μm with 1.6 μm with 2.25 μm	No	Bi-phasic
Exp 3: Investigate the impact of intra-phase temperature heterogeneity.	Tri-phasic	Threshold VIIRS-NGT SLSTR-NGT Comm-NGT VIIRS-Day	Vary	Bi-phasic

4.1.2. Bayesian Estimation Implementation

We employed an MCMC algorithm to estimate fire parameters under a Bayesian framework. In this approach, a predefined parametric model defines both the likelihood function and the prior distributions. From Bayes theorem, these can be combined to form the posterior distribution from which samples of the parameters of interest are drawn (cf. equation 9). As summarized in Table 2, we evaluated three fire parametric assumptions, mono-phasic (MP), bi-phasic (BP), and tri-phasic (TP), all based on the finite-phase radiance formulation in Eqn. 3. These models were used to address the core OSSE questions outlined earlier in this section. The priors for each model's parameters are detailed in Table 3.

Table 3: Priors adopted by the parametric models used in retrieval

	Temperature prior	Fractional area
Mono-phasic	$\bar{T} \sim U(350, 1800)$	$\log\ \bar{a} \sim U(-6, 0)$
Bi-phasic	$T_s \sim U(350, 900)$	$\log\ a_s \sim U(-6, 0)$
	$T_f \sim U(900, 1800)$	$\log\ a_f \sim U(-6, 0)$
Tri-phasic	$T_R \sim U(350, 460)$	$\log\ a_r \sim U(-6, 0)$
	$T_s \sim U(460, 900)$	$\log\ a_s \sim U(-6, 0)$
	$T_f \sim U(900, 1800)$	$\log\ a_f \sim U(-6, 0)$

There are several standard MCMC sampling strategies, including the Metropolis algorithm (Gelman et al., 1995), Hamiltonian Monte Carlo (HMC, Betancourt, 2017), and their various extensions. The Metropolis algorithm is a classical method that uses a proposal distribution to generate candidate samples, which are then accepted or rejected based on an acceptance probability. Although relatively simple and effective in low-dimensional problems, its performance can degrade in higher-dimensional spaces or if the proposal distribution is poorly tuned. In contrast, HMC incorporates concepts from classical mechanics, using simulated Hamiltonian dynamics to generate more efficient proposals that explore the parameter space more effectively.

HMC typically reduces autocorrelation and improves convergence in high-dimensional problems. However, it requires evaluation of gradients of the log-posterior, which may be computationally expensive or unavailable in certain models. In addition, HMC performance is sensitive to tuning parameters such as step size and the number of leapfrog steps.

In this research, we adopted an adaptive variant of HMC, the No-U-Turn Sampler (NUTS, Hoffman et al., 2014), as our primary sampling strategy. NUTS eliminates the need for manual tuning of trajectory length by adaptively determining the number of leapfrog steps, making it particularly suitable for complex, high-dimensional models. However, it still relies on smooth gradient information to simulate Hamiltonian dynamics. In our case, the use of truncated priors (Table 3) imposes hard bounds on parameter spaces, potentially introducing discontinuities or non-smooth regions in the posterior. These can lead to unstable or undefined gradients near the boundaries, causing leapfrog integrator failure and violating the *no U-turn* condition, thereby reducing sampling efficiency or preventing convergence. For cases where NUTS fails due to gradient issues, we revert to the Metropolis algorithm as a fallback. To mitigate the Metropolis sampler's sensitivity to initialization, we first compute the maximum-a-posteriori (MAP) estimate using the Limited-memory Broyden–Fletcher–Goldfarb–Shanno Bounded (L-BFGS-B) optimization algorithm (Zhu et al., 1997). This MAP estimate is then used as the starting point for the Metropolis sampler to draw posterior samples.

During the tuning phase, all samplers are allowed up to 2,000 iterations to optimize their settings for efficient posterior exploration. These tuning samples are discarded, as they do not represent the equilibrium distribution. After tuning, we retain 2,000 samples from the posterior for each case study to support subsequent parameter inference and uncertainty quantification.

4.1.3. Evaluation metrics

The objective of sub-pixel fire characterization is to retrieve a representative set of fire temperatures and their fractional areas that approximate the true temperature–area distribution within a satellite pixel. These estimated parameters must satisfy two key criteria. First, they should achieve radiative closure, that is, the reconstructed radiance signal, derived from the estimated temperature-phase combinations, should closely match the observed radiance in the channels used for retrieval, within observational uncertainties. Second, the retrieved parameters must be physically meaningful beyond fitting the observed spectrum, enabling the derivation of other fire-relevant properties, such as total fire energy and phase-specific heat fluxes.

To evaluate these two aspects, we use four field-of-view (FOV) metrics tied to biomass-burning emissions and plume injection processes. The first is the FRP derived from temperature retrieval ($\mathcal{F}_{\mathrm{T}}$), which quantifies the total radiative energy output of the fire and is given by:

$$\mathcal{F}_{\mathrm{T}} = A\pi \int_{-\infty}^{+\infty} L(\lambda) d\lambda = A\sigma \sum_{i=1}^{N} a_i T_i^4 \tag{10}$$

Here, $\sigma = 5.670374419 \times 10^{-8}$ W m^{-2} K^{-4} is the Stefan–Boltzmann constant, N is the number of temperature components (fire phase), and A is the pixel area, assumed to be the VIIRS M-band nadir footprint of 750 m × 750 m in this paper. It is worth noting that FRP is also derived operationally using regression-based methods based on the 4 μm fire radiance which is used as a proxy for estimating T^4 (e.g., $T^4 \approx L_4(T)/C$, where C is the empirical regression coefficient). For example, the standard VIIRS active fire product uses the Wooster approach:

$$\begin{aligned} \mathcal{F}_{\mathrm{W}} &= A\sigma \frac{(L^{\mathrm{M13}} - L^{\mathrm{M13b}})}{C} \\ &= A\sigma \sum_{i=1}^{N} \frac{a_i (L_i^{\mathrm{M13}} - L^{\mathrm{M13b}})}{C} \approx A\sigma \sum_{i=1}^{N} a_i T_i^4 \end{aligned} \tag{11}$$

where L^{M13} is the observed radiance in the 4 μm channel (M13), L^{M13b} is the background radiance, and C is a channel-specific coefficient. For VIIRS band M13, $C = 2.88 \times 10^{-9}$ W m^{-2} sr^{-1} μm^{-1} K^{-4}.

While the retrieved FRP reflects the total fire energy (i.e., the area under the radiance curve in Fig. 1), it does not necessarily ensure that the spectral shape is accurately captured. This limitation is evident in the flaming and smoldering examples in Fig. 1, which exhibit similar FRP values but differ substantially in their spectral distributions. Therefore, we also use the Visible Energy Fraction (VEF, $\mathcal{V}$), introduced by Wang et al. (2020a), to assess spectral variability:

$$\mathcal{V} = \frac{A\pi \int_{\lambda_u}^{\lambda_l} L(\lambda) d\lambda}{\mathcal{F}_{\mathrm{W}}} \propto \frac{L^{\mathrm{DNB}}}{L^{\mathrm{M13}}} \tag{12}$$

where $\lambda_l = 0.5$ μm and $\lambda_u = 0.9$ μm, corresponding to the VIIRS DNB bandpass.

To further assess the retrieved flaming-phase temperatures and fractional areas, we also evaluate the ability of the retrievals to represent flaming heat fluxes. Specifically, from the posterior samples we compute the flaming radiative heat flux (Q_f^{rad}) and convective heat flux (Q_f^{conv}, Liu et al., 1979; Freitas et al., 2007), which are relevant for plume rise and injection height modeling:

$$Q_{\text{rad}}^{f} = \frac{\sigma \sum_j^J a_{f,j} T_{f,j}^4}{\sum_j^J a_{f,j}} \tag{13}$$

$$Q_{\text{conv}}^{f} = \rho c_p C_H U \left(\frac{\sum_j^J a_{Fj} T_{f,j} T_{2m}}{\sum_j^J a_{Fj}} - T_{2m} \right) = \alpha \frac{\sum_j^J a_{Fj} \Delta T_{f,j}}{\sum_j^J a_{Fj}} \tag{14}$$

Here, J is the number of flaming temperature components, $\rho \approx 1.2\ kg \cdot m^{-3}$ is air density, $c_p \approx 1005\ J \cdot kg^{-1} \cdot K^{-3}$ is air density, C_H is turbulent (bulk) heat transfer coefficient, and U is characteristic wind speed

The MCMC algorithm yields posterior samples of fire model parameters (e.g., T_s, p_s, T_f, p_f for the bi-phasic model). These parameter samples are first used to compute the relevant physical parameters (i.e., $\mathcal{F}_T$, $\mathcal{V}$, Q_{rad}^{f}, and Q_{conv}^{f}), from which we form the corresponding posterior distributions. In what follows, the mode of these distributions are used for comparison with the ground truth.

4.2. Experiment 1: Assessing the Impact of Temperature Phases

As summarized in Table 2, for this experiment we employ a tri-phasic, intra-phase heterogeneous model for the nature run. Each temperature phase (flaming, smoldering, and residual) was represented by 10 sub-phase members sampled based on the sampling strategy described in Section 4.1.1 with a temperature variation of 100 K. Under the uniform hyper-spectral (USS) band configuration, fire radiance is simulated across 115 spectral channels, offering sufficient degrees of freedom to decouple phase-channel interactions and isolate the effects of model complexity. Zero-mean Gaussian noise is added to each channel, with the standard deviation set to 5% of the signal amplitude. Using this nature run, we evaluate three parametric fire models for the MCMC retrievals: mono-phasic (MP), bi-phasic (BP), and tri-phasic (TP) to assess their performance in sub-pixel fire characterization. Fig. 2 shows the posterior distributions and the 95% Highest Density Intervals

(HDIs) for the estimated parameters under each model, corresponding to the smoldering case in Fig. 1. HDIs represent the narrowest interval containing a specified portion (e.g., 95%) of the posterior probability mass, with every point inside the interval having higher probability density than those outside. When assessing retrieval uncertainties, the use of HDIs is favored over standard deviations because the posterior is often not gaussian. In Fig. 2c–l, blue dashed lines mark the ground-truth means used for sub-phase temperature sampling. This comparison is unavailable for mono-phasic model since it retrieves only a single temperature and fractional area, precluding direct comparison.

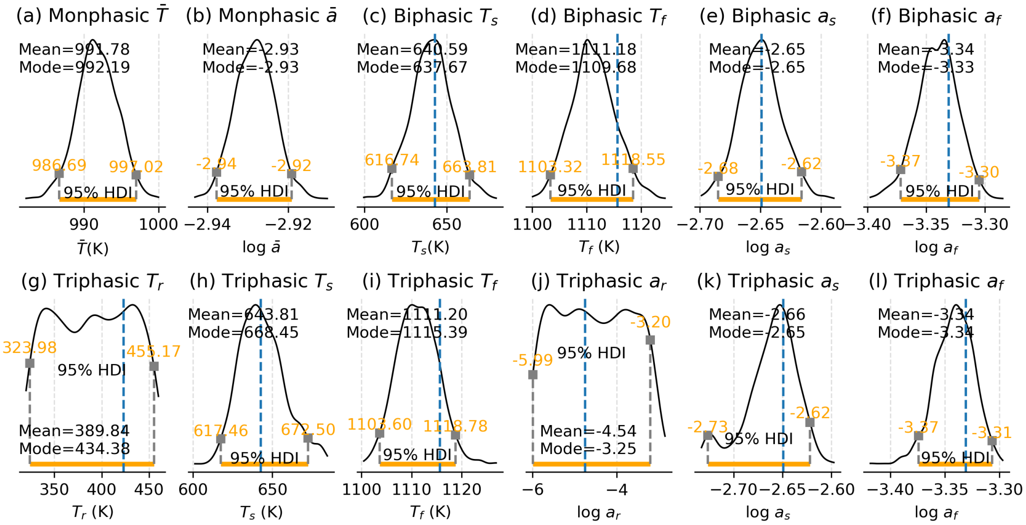

Figure 2: Posterior distribution and the 95% Highest Density Interval of the subpixel fire characterization using mono-phasic, bi-phasic, and tri-phasci model for the given smoldering fire illustrated in Fig. 1. (a)-(b) are the distributions of mono-phasic parametric model assumption, (c)-(f) are for bi-phasic, and (h)-(l) are for tri-phasic.

As shown in Fig. 2, most parameter posteriors appear bell-shaped, indicating stable inference and identifiable modes. For the BP and TP cases, the ground-truth modes fall within their respective HDIs, confirming that the MCMC algorithm effectively captures posterior uncertainty and recovers physically meaningful estimates. Notice that the algorithm struggles estimating the residual temperature (T_r) and area fractions (a_r) (Fig. 2g and 2j).

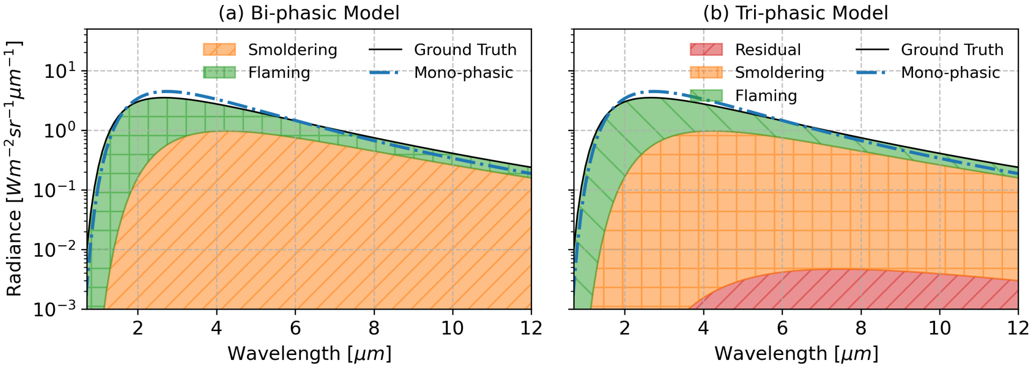

Figure 3: The reconstructed spectral radiance for the given smoldering fire illustrated in Fig. 1. (a) Spectral radiance estimated under the bi-phasic parametric fire model; (b) Same as (a) but is estimated under the tri-phasic. The colored stacked areas depict the contribution of each assumed fire phase. The spectral radiance estimated under mono-phasic assumption are denoted as the blue broken line in (a) and (b). The black solid lines are the ground truth fire signal.

Using the posterior samples, we reconstruct the spectral radiance for each parametric model assumed in the retrievals. Figure 3 compares the radiance derived from the BP (a) and (b) TP models (stacked colored areas) against the ground-truth spectrum (black line). The MP-retrieved spectrum is also shown in each one of these diagrams as blue dashed line. The colored stacked areas depict the contribution of each assumed fire phase (e.g., flaming, smoldering, and residual), if applied, to the total radiance. As shown, when the retrieval uses the BP and TP models, the reconstructed radiances closely match the spectral shape of the true signal (the black curve is nearly identical to the stacked plots.) In contrast, the MP model (blue dashed line) underestimates radiance at wavelengths below 1.6 μm and above 6.5 μm, while overestimating in the mid-wave range (1.6∼6.5 μm). Table 4 summarizes the evaluation metrics for this case, including relative errors provided in parentheses. Although all three models provide some level of accuracy, MP performs the worst. Despite exhibiting narrow HDIs (Fig. 2a,b), MP overestimates FRP by 6.39% and underestimates VEF by 31.2%. Moreover, MP lacks the ability to partition phase-specific contributions and therefore cannot estimate flaming-phase heat fluxes.

By contrast, the BP and TP models better capture spectral variability, especially in the visible band. For example, both models retrieve a high-temperature flaming phase (≈ 1110 K) with a fractional area of 0.05%, increasing visible radiance from 0.09 to 0.29 W m^{-2} sr^{-1} μm^{-1}and reducing 4 μm radiance from 3.69 to 3.09 W m^{-2} sr^{-1} μm^{-1}. As a result, VEF errors improve from -31.2% (MP) to -0.04% (BP) and -0.08% (TP). Since FRP can be computed as the integral of spectral radiance (Eqn. 10), a more accurate spectral shape leads to improved FRP estimates: the relative error drops from 6.39% (MP) to 0.05% (BP) and 0.09% (TP). Furthermore, BP and TP enable reliable estimation of phase-partitioned flaming heat fluxes (Q_f^{rad} and Q_f^{conv}), both retrieved with negligible error.

Table 4: configurations of the non-homogeneous fire model

[1]Model	[2]FRP	ln VEF	Q_f^{rad}	[3]Q_f^{conv}
Truth	60.83	-4.19	1.51	$\alpha\times$798.81
MP	64.72(6.39%)	-5.50(-31.2%)	-	-
BP	60.86(0.05%)	-4.20(-0.04%)	1.52(0.86%)	$\alpha\times$801.20(0.22%)
TP	60.88(0.09%)	-4.20(-0.08%)	1.52(0.87%)	$\alpha\times$801.23(0.22%)

[1] MP stands for mono-phasic, BP is bi-phasic, and TP is tri-phasic;

[2] The unit for FRP is MW; for Q^f_{rad}, it is in $\times$ 10^{12} Wm^{-2}; for Q^f_{conv}, it is in $\times$ 10^3 Wm^{-2};

[3] α is an arbitrary heat transfer coefficient.

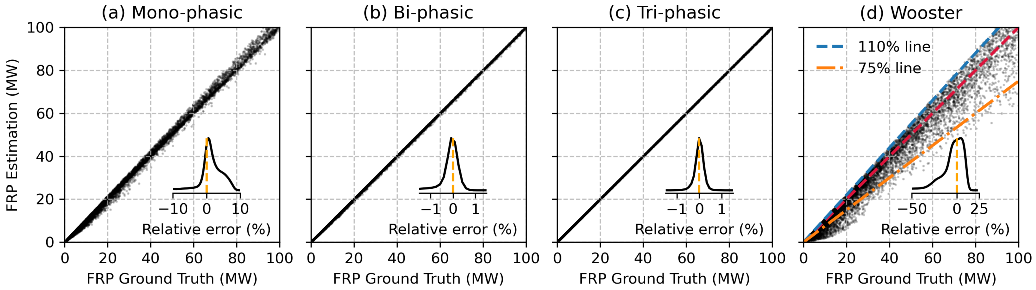

Figure 4: Scatter plots that compares the Fire Radiative Power (FRP) derived by different method against the ground truth. (a) FRP derived from the subpixel fire parameters based on the mono-phasic parametric assumption comparing against the ground truth; (b) Same as (a), but for fire parameters under the bi-phasic parametric assumption; (c) for tri-phasic; (d) for FRP derived using Wooster's empirical regression technic. The inset plots are the distribution of relative error.

We also conducte systematic assessments across the OSSE ensemble using the parameters introduced in Section 4.1.3. Fig. 4 presents the FRP evaluation results, focusing on the 0∼100 MW range, typical of wildfire pixels observed by moderate-resolution sensors. As demonstrated, all three models exhibit high overall accuracy. However, consistent with the case study, MP produces FRP overestimates of up to 10%, whereas BP and TP keep errors within 1%. Notably, even with this overestimation, MP still outperforms Wooster's regression-based FRP method.

Figure 4d shows that the Wooster's approach underestimates FRP significantly, with errors up to 80% for FRP values below 30 MW. This discrepancy is analyzed in Fig. 5. In Fig. 5a, the 4 μm radiance (green stars) is a monotonic function of T^4 (green line), although the relationship does not appear linear. Recall that the Wooster FRP estimator (Eq. 11) fundamentally relies on the linear relationship between $L_4(T)$ and T^4, with an empirical scaling factor connecting the two. However, it is apparent that the relationship is neither perfectly linear nor exactly aligned. Fig. 5b further explored the nonlinearity and temperature dependency between $L_4(T)$ and T^4. Here, the red line represents the linear mapping $(L_4(T)/C)$ used in Wooster's approach, using $C = 2.88 \times 10^{-9}\text{Wm}^{-2}\text{sr}^{-1}\mu\text{m}^{-1}\text{K}^{-4}$ for VIIRS M13 band. The green line depicts the ratio between the linear approximation $(L_4(T)/C)$ and the actual T^4. As shown, Wooster's method overestimates FRP by up to 13% for fires within the temperature range of 700∼1200 K. Conversely, outside this range, particularly for fires cooler than 400 K, the method significantly underestimates FRP, with errors reaching 80% or more.

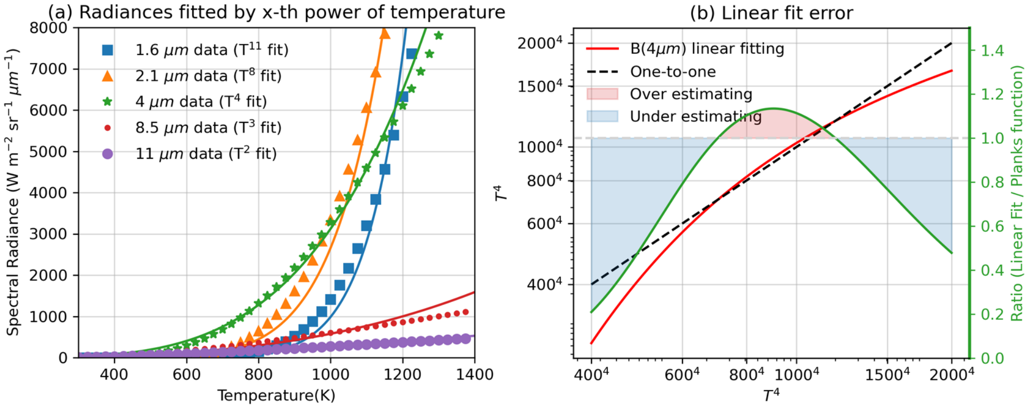

Figure 5: Diagnosing of the uncertainty of Wooster's approach for FRP estimation. (a) Band radiance fitted by different power of temperature. (b) Illustration of the uncertainty introduced to FRP estimation by the linear fitting of Stefan-Boltzmann Law. The axis ticks in (b) are present in T^4 scale for better interpretation.

Fig. 6 evaluates VEF, Q_f^{rad}, and Q_f^{conv}. As expected, the mono-phasic model (MP) struggles with VEF, particularly in mixed-phase fires where the flaming and the cooler components (smoldering and residual) are comparable. In these scenarios, MP's VEF estimates deviate sharply from the one-to-one line, reflecting its limited degrees of freedom for capturing spectral complexity, even when provided with abundant observational data. In contrast, both the BP and TP models yield accurate VEF estimates. The VEF values estimated by the BP model display slightly greater dispersion compared to those from the TP model, particularly in scenarios where the MP estimates exhibit large discrepancies. Even in the worst cases, BP's relative VEF error remains within 2.5%, which is acceptable for most applications. Estimates for Q_f^{rad} and Q_f^{conv} follow similar trends. BP and TP models yield comparably small relative errors ($< 2.5\%$), though BP exhibits slightly more spread. These results reaffirm that multiphasic models—particularly BP—are better suited for sub-pixel fire characterization when spectral variation is significant.

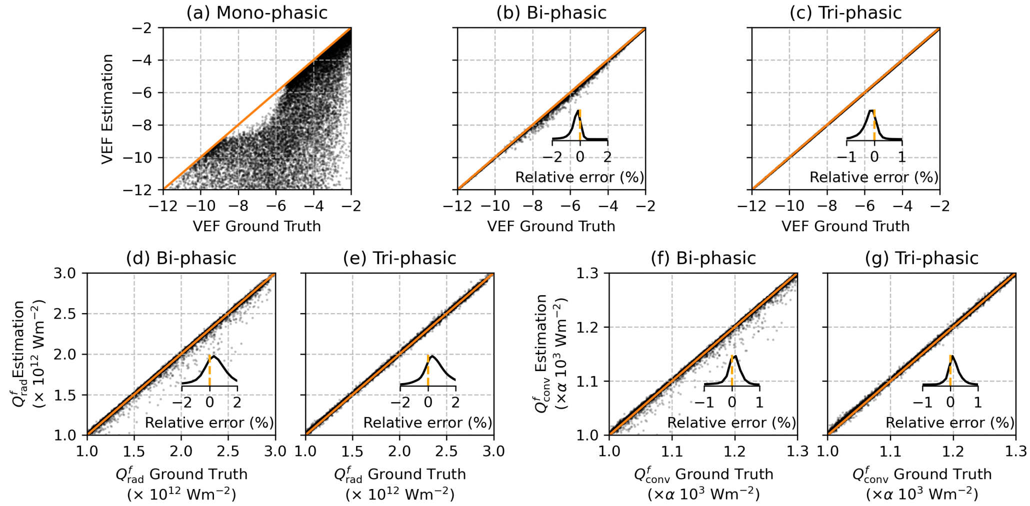

Figure 6: Scatter plots that compares the visible energy fraction (VEF), flaming radiative heat flux Q^f_{rad} and convective heat flux (Q^f_{conv}) derived by different parametric fire assumption against the ground truth. (a) - (c) VEF comparison of the VEF for the three parametric fire assumptions. (d) and (e) are the Q^f_{rad} under bi-phasic and tri-phasic assumptions. (f) and (g) same as the (d) and (e) but for Q^f_{conv}. The inset plots are the distribution of relative error.

Summary. This experiment isolated the effect of model complexity by using a high-information (115 observational channels), noise-perturbed simulation. Key findings include: (1) FRP derived from temperature retrievals (MP, BP, or TP) consistently outperforms the Wooster regression method, especially for low-intensity fires; (2) MP shows the largest errors in FRP and VEF, highlighting its inadequacy for heterogeneous fire scenarios; (3) While the TP model showed slightly better performance compared to the BP model, the improvement in estimation accuracy was marginal across all evaluated metrics.

Given practical constraints, where the available observational data are typically limited (<10 channels) and may not be sufficient to adequately constrain the tri-phasic (TP) model, the bi-phasic (BP) model emerges as the most pragmatic choice. Thus, the bi-phasic model will serve as the primary parametric model for sub-pixel fire characterization in the subsequent sections.

4.3. Experiment 2: Assessing the Impact of Channel Selection

For this experiment, we use a bi-phasic fire model for both the nature run and for the MCMC retrieval algorithm. We then explore several choices of channel selection and assess their ability to constrain sub-pixel fire characterization. We introduce random noise into the simulated fire signal, following the signal-to-noise ratio (SNR) characteristics of VIIRS (Cao et al., 2013), implicitly ignore forward model errors. While this OSSE setup allows direct comparisons of temperature and fractional area estimates against the ground truth, we adhere to the four selected evaluation parameters. The primary objective of this OSSE is to understand the information content of each available channel in constraining sub-pixel fire properties. Using these standardized metrics ensures straightforward intra-OSSE comparisons and facilitates understanding of parameter uncertainties when observational constraints are limited.

Impact of individual channels on derived fire properties. Fig. 7 illustrates the likelihood of each selected band for the smoldering fire case shown in Fig. 1. The fire signal is generated under the Best-NGT band configuration. For illustration purposes, we use the 4 μm and 10.5 μm observations used into the bi-phasic model (Eq. 7) and explicitly solve for a_S and a_F. This device allow us to compute posteriors (Eq. 9) as a function of T_s and T_f which are easier to visualize in 2 dimensions. As depicted in Fig. 7, the visible

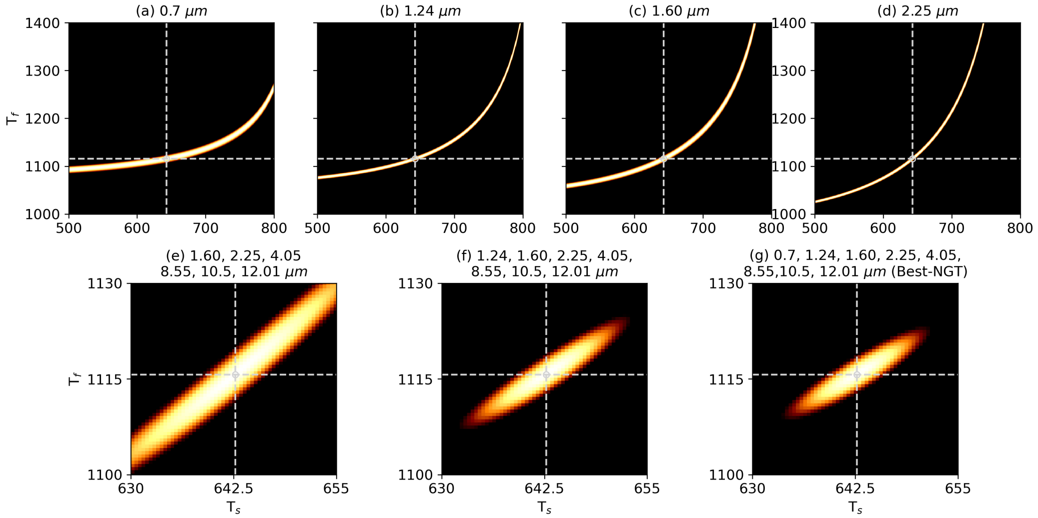

Figure 7: The likelihood of (a) DNB, (b) 1.24 μm, (c) 1.60 μm, (d) 2.25 μm, and the joint-likelihood for the band of (e) 1.60 μm, 2.25 μm, 4.05 μm, 8.55 μm, 10.5 μ, and 12.01 μm, (f) 1.24 μm, 1.60 μm, 2.25 μm, 4.05 μm, 8.55 μm, 10.5 μ, and 12.01 μm, (g) Best-NGT (DNB, 1.24 μm, 1.60 μm, 2.25 μm, 4.05 μm, 8.55 μm, 10.5 μ, and 12.01 μm). the axis of (e) to (f) are zoomed in for better visualization. Observations from 4.05 and 12.01 μm are used to solve the a_s and a_f for the given combination of T_s and T_f following the standard BSDM approach.

DNB (0.7∼0.9 μm) provides the strongest constraint on flaming temperature estimation among the selected bands. However, it also exhibits limited ability to constrain smoldering temperature, as indicated by the broad spread in the marginal likelihood of T_s in Fig. 7a. Conversely, at longer wavelengths, the constraint on flaming temperature weakens, whereas the constraint on smoldering temperature improves. Consequently, integrating all available channels significantly reduces the solution space for both T_s and T_f, as demonstrated by the joint likelihood, which peaks near the true values shown as Fig. 7g. (Notice that Figs. 7e-g have zoomed in axis.)

It is important to note that the likelihood values in this analysis depend on the calculation of a_s and a_f, a device that was adopted for illustration purposes. In the supplementary material (Fig. A.13), we present an alternative setup in which 1.6 μm and 10.5 μm radiance are used to solve for a_s and a_f. Under this configuration, the added information from 1.24 μm and 2.25 μm is comparable to, or even superior to, that of 0.7 μm. While these results reaffirm the importance of shorter wavelengths in constraining the solution space, it also suggests that the more general MCMC algorithm that we implement, one that simultaneously solves for temperatures and fractional areas, better integrates the available information and further reduce uncertainties.

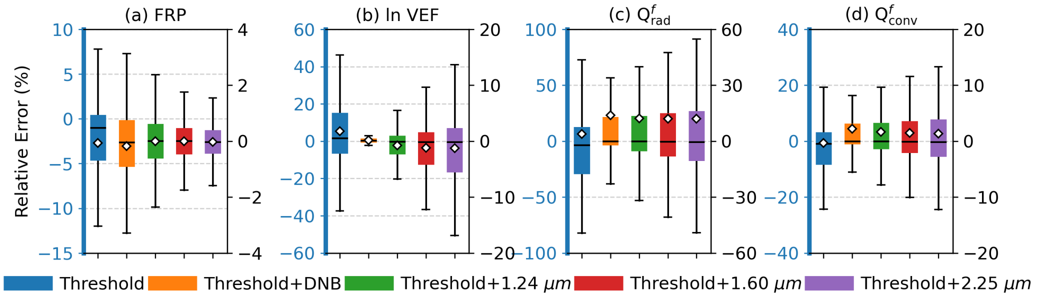

Figure 8: Box plots of the relative error of the selected retrieved fire properties under the bi-phasic fire parametric assumption. The threshold band configuration includes 4.05 μm, 8.55 μm, 10.5 μm, and 12.02 μm channels. The selected channels are added individually into the threshold configuration to assess the value added of each channel in sub-pixel fire characterization. Orange represents adding DNB (0.7∼0.9 μm) to threshold; Green is for adding 1.24 μm to threshold; Red is for 1.6 μm; and purple is for 2.25 μm. The range of the threshold relative error are on the left Y-axis, and the rests are on the right Y-axis.

Impact of individual channels on derived fire properties. To quantitatively assess the added value of each channel in sub-pixel fire characterization, we evaluate the four selected parameters under single-channel additions. Starting from the threshold configuration, we conduct separate experiments where one additional channel is added at a time. The relative error distribution in each metric is then evaluated to assess the contribution of each added channel. Fig. 8 summarizes the statistical evaluation by means of box plots. Under the BP parametric model, the threshold channel configuration provides very limited skill in reconstructing the fire properties. Estimated temperatures result in up to 50% errors in both $\ln(\mathcal{V})$ and Q^f_{rad}. As additional channels are introduced, the relative errors in all four metrics progressively decrease. The FRP estimation error is reduced to 2% when including the 2.25 μm band, while the VEF estimation error is minimized to 1% when incorporating the DNB band.

Interestingly, the FRP uncertainties behave differently than the other fire properties when observations with longer wavelength are added. As shown in Fig. 8a, longer wavelengths contribute more significantly to suppressing

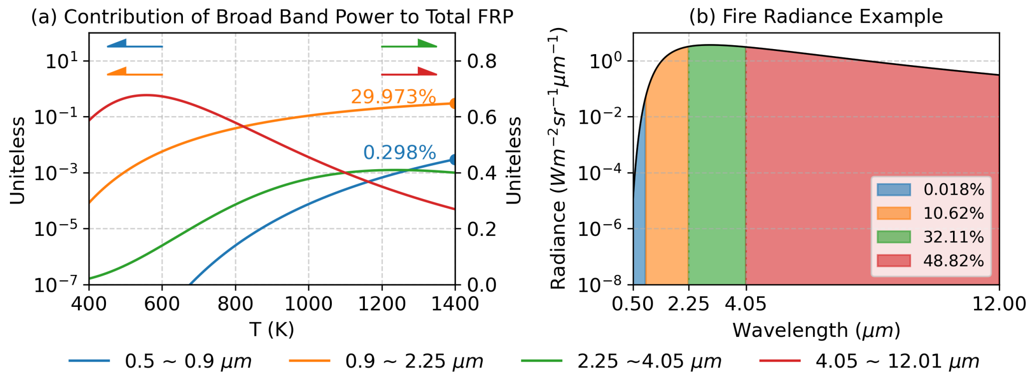

Figure 9: Diagnosing the impact of adding different spectral bands on FRP estimation: (a) Broadband power contribution to total FRP estimation as a function of burning temperature, (b) radiance as a function of wavelength for the smoldering fire example in Fig. 1. The four color used in (b) represent the four spectral ranges over the course of the 0.5 to 12 μm, with blue for 0.5∼0.9 μm, orange for 0.9∼2.55 μm, green for 2.25∼4.05 μm, and orange for 4.05∼12 μm. The contribution of the 0.5∼0.9 μm and 0.9∼2.55 μm are illustrated in log-scale (left Y-axis of (a)). 2.25∼4.05 μm and orange for 4.05∼12 are in linear scale (left Y-axis of (a)).

FRP estimation errors, whereas shorter wavelengths provide stronger constraints for the other metrics. This contrasting behavior can be explained by analyzing the broadband power contribution to total FRP in Fig. 9a. Over the entire biomass-burning temperature range, the visible band contributes at most 0.3% to total FRP, whereas the 2.1∼4.0 μm range contributes up to 40%. As additional bands are incorporated, the derived temperatures first regulate the overall spectral variation of the fire radiance, leading to general improvements in FRP estimation relative to the threshold scenario. Specifically, adding the 2.1 μm band significantly reduces spectral variation in the 2.1 μm range, which contributes substantially to FRP, thereby yielding the largest reduction in FRP estimation error. In contrast, while the DNB band constrains overall spectral variation, it leaves a broader range of unconstrained wavelengths, many of which contribute significantly to FRP. As a result, adding DNB is less effective in improving FRP estimation.

Fig. 8b also highlights that adding DNB imposes the strongest constraint on VEF estimation, which is expected given that VEF is derived directly from DNB radiance. A temperature estimate constrained by DNB should yield smaller errors in reproducing DNB radiance, leading to the least VEF estimation error compared to other configurations. Furthermore, when combined with the evaluation of Q^f_{rad} and Q^f_{conv}, Fig. 8 suggests that adding DNB enhances flaming temperature partitioning. This finding is consistent with Fig. 7, where DNB effectively reduces the solution space for flaming temperature. This behavior arises because DNB is largely insensitive to temperatures below 900 K; for the DNB, $\partial P(T, \lambda)/\partial T$ below 900 K is up to eight orders of magnitude smaller than above 900 K (see Fig. A.14 in the supplemental material). Consequently, temperature variations in the smoldering range have minimal impact on the DNB likelihood, making DNB largely unresponsive to smoldering temperature. On the other hand, Fig. A.14 also reveals that $\partial P(T, \lambda)/\partial T$ for the 2.1 μm band exhibits a smaller dynamic range, indicating a stronger ability to constrain smoldering temperature but a weaker ability to constrain flaming temperature, consistent with the observations in Fig. 7d. This also explains why, in Figs. 8b∼d, the relative errors in $\ln(\mathcal{V})$, Q^f_{rad}, and Q^f_{conv} are higher when adding longer-wavelength bands such as 1.24 μm, 1.60 μm, or 2.25 μm compared to when adding DNB.

Summary. This section evaluates the role of different spectral channels in constraining sub-pixel fire characterization under a bi-phasic fire model. The results show that while shorter-wavelength channels (e.g., DNB) impose stronger constraints on flaming temperature, they provide limited information on smoldering components. Conversely, near infrared channels (e.g., 2.25 µm) contribute more to FRP estimation by capturing spectral variations in wavelength ranges critical to FRP.

4.4. Experiment 3: Assessing the Impact of Intra-phase Temperature Heterogeneity

In practice, wildfire temperature distributions are rarely homogeneous; assessing the impact of this heterogeneity on retrievals is therefore essential. Following the configurations in Section 4.2, we employ a tri-phasic nature run with intra-phase temperature variation ranging from 0 K (homogeneous) to 300 K in 50 K increments. All bands use VIIRS spectral response functions and band-specific noise. We evaluate USS, BEST-NGT, and VIIRS-NGT against a threshold configuration (Section 4.3) and a VIIRS-Day setup. We present two analyses: a full-scenario evaluation (Supplementary) and a flaming-focused scenario (main text). Because smoldering-dominated fires generally inject within the PBL, errors in flaming-phase parameters have limited effect on injection height; in contrast, plume rise in flaming-dominated scenes depends strongly on flaming temperature and area. Accordingly, we

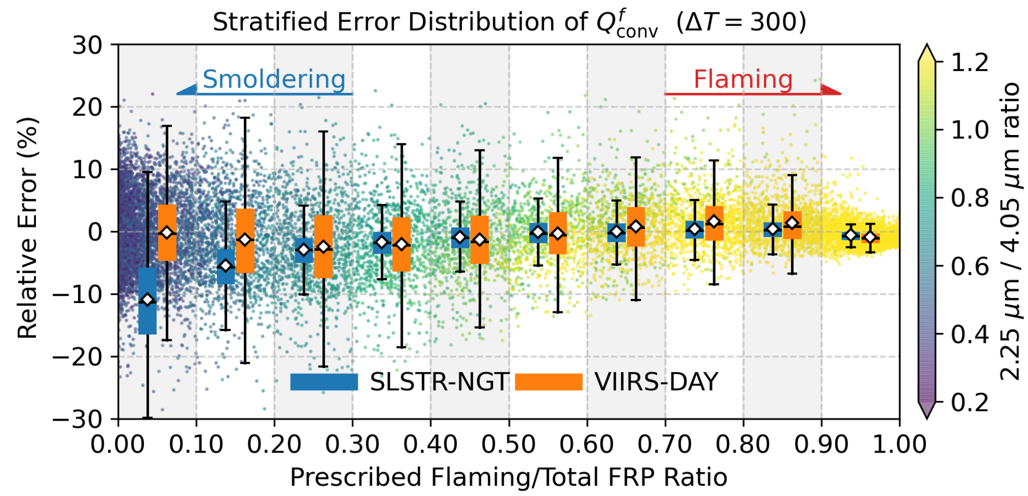

Figure 10: Stratified error distribution of the convective flaming heat flux (Q^f_{conv}) at 300 K intra-phase temperature heterogeneity, for SLSTR-NGT (blue) and VIIRS-Day (orange). Bins are defined by the flaming-to-total FRP ratio (10 quantiles). Background points show the radiance ratio $R_{\mathrm{NIR}} \equiv L_{2.25\,\mu\mathrm{m}}/L_{4.05\,\mu\mathrm{m}}$ for each OSSE case, which correlates with the FRP ratio and serves as a practical proxy for screening smoldering-dominated pixels.

define and validate a screening criterion, analyze stratified errors (Fig. 10), and then show filtered summaries (Fig. 11); full distributions appear in the Supplementary.

Fig. 10 shows that Q^f_{conv} errors are largest when smoldering and residual phases dominate (low flaming FRP fraction). Performance improves markedly once the flaming fraction exceeds ~ 0.2 for SLSTR-NGT, and more gradually for VIIRS-Day. Because the true flaming fraction is not directly observable in a single snapshot, we use the band ratio

$$R_{\mathrm{NIR}} \equiv \frac{L_{2.25\,\mu\mathrm{m}}}{L_{4.05\,\mu\mathrm{m}}}$$

as a practical proxy to flag heavily smoldering cases. A simple screen of $R_{\mathrm{NIR}} > 0.2$ and FRP $> 20\,\mathrm{MW}$ effectively isolates these scenes (points in Fig. 10). This filtering is both practical and meaningful because smoldering-dominated fires typically inject within the boundary layer, where plume-rise parameterizations are less sensitive to flaming-phase properties; detailed flaming retrievals are therefore less critical for such cases.

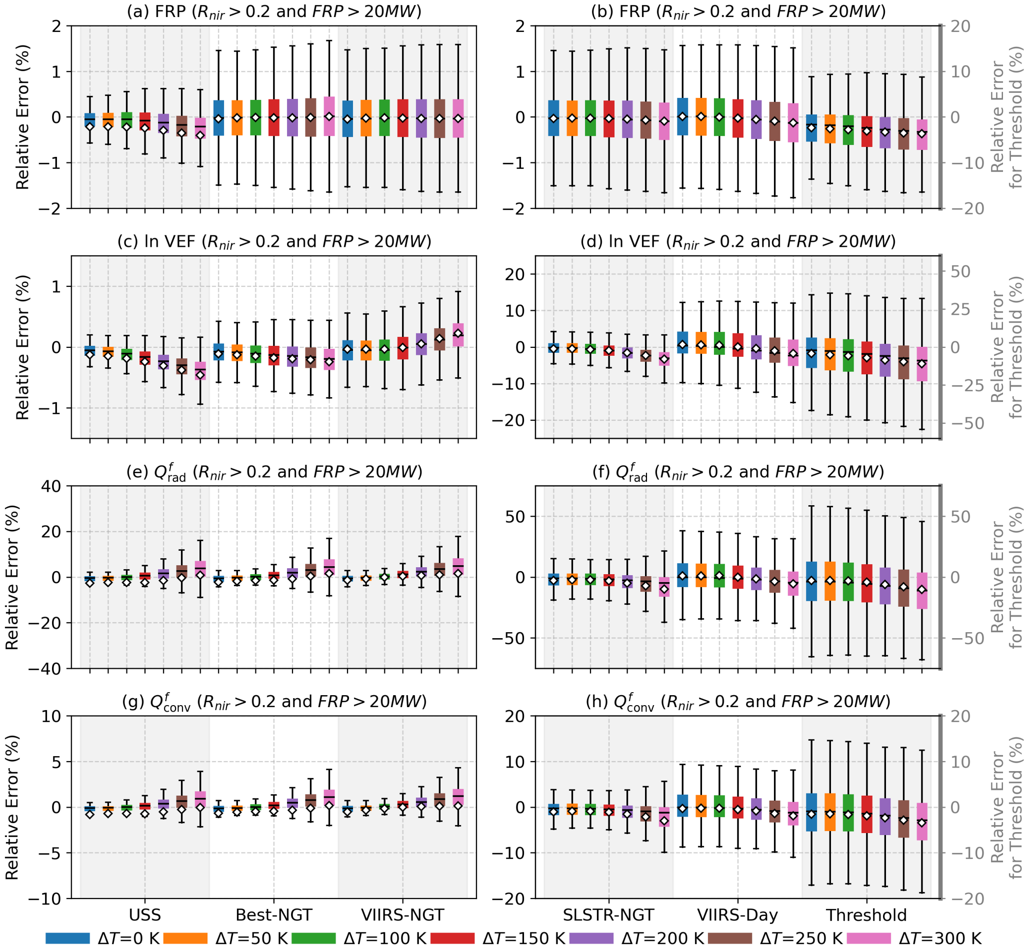

Figure 11: Statistic summary of the evaluation of OSSEs using the proposed four quantities for investigating impact intra-phase temperature heterogeneity with smoldering dominated fire filtered. Seven levels of temperature variation are investigated and are denoted as blue for 0 K, orange for 50 K, green for 100 K, red for 150 K, purple for 200 K, brown for 250 K, and pink for 300 K. Six band configurations are considered. The error range for the threshold band configuration are shown left Y-axis of (b), (d), (f), and (h). See text for details.

Applying this screen leads to a marked contraction of the error distributions across configurations (Fig. 11) relative to the full-scenario results (Fig. A.15). Consistent with earlier findings, FRP remains highly resilient to both increasing intra-phase variability and reduced band counts. Across enhanced configurations, i.e., those with additional bands beyond the threshold—FRP relative errors stay within ∼2% in both the flaming-focused scenario (Figs. 11a,b) and the full scenario (Figs. A.15a,b). Much of the improvement over the threshold configuration is attributable to the 2.25 μm band: BEST-NGT and VIIRS-NGT show little additional FRP gain over VIIRS-Day despite including shorter bands (DNB, 1.24, 1.60 μm), indicating that 2.25 μm provides the dominant incremental constraint on FRP.

USS, BEST-NGT, and VIIRS-NGT also recover $\ln(\mathcal{V})$ with relative errors below ∼1% for the flaming-focused scenario; omitting shortwave observations degrades performance substantially: SLSTR-NGT (no DNB and 1.24 μm) reaches errors up to 10%, and VIIRS-Day can reach ∼15% when only 2.25 μm constrains the shortwave side (300 K variability). Increasing intra-phase variation raises overall errors and introduces configuration-dependent biases, negative for USS, reduced for BEST-NGT, and slightly positive for VIIRS-NGT, consistent with band-specific temperature sensitivities (mechanistic details in Figs. A.17–A.16). Although VIIRS-Day can exhibit ∼15% error in $\ln(\mathcal{V})$, the implied MCE bias is small because MCE $\approx 1 + 0.017\ \ln(\mathcal{V})$ (Wang et al., 2020a; Zhou et al., 2023); for $\ln(\mathcal{V}) \in [-12, -3]$, this maps to ≤ 0.003 (i.e., $\leq 0.3\%$) absolute MCE error.

The radiative and convective heat fluxes, Q^f_{rad} and Q^f_{conv}, are most sensitive to both temperature variability and channel selection because they depend on phase partitioning rather than total radiance alone; thus, insufficient constraints can yield poor partitioning even when the overall spectral shape is well matched. As expected from the T^4 scaling, Q^f_{rad} exhibits a wider error range than Q^f_{conv}. For USS, BEST-NGT, and VIIRS-NGT, Q^f_{conv} relative errors are generally below 5% for the flaming-focused scenario, reflecting the strong constraint provided by VIIRS DNB on temperature partitioning. For SLSTR-NGT and VIIRS-Day, errors are typically $\lesssim$10%, highlighting the limited ability of longer near-infrared bands (1.6 and 2.25 μm) alone to resolve phase temperatures.

For completeness, in the *full (unfiltered) scenario* the same qualitative ordering holds: FRP remains within ∼2% across enhanced configurations, while $\ln(\mathcal{V})$ errors increase when shortwave constraints are reduced (SLSTR-NGT up to ∼10%; VIIRS-Day up to ∼15% at 300 K). Heat-flux errors broaden due to phase-partitioning ambiguity, with Q^f_{rad} wider than Q^f_{conv} (allowable-error envelopes in Table A.5; full distributions in Fig. A.14).

Summary. This section assesses the impact of intra-phase temperature heterogeneity on sub-pixel fire characterization under a bi-phasic model. We find that: (i) FRP is robust to intra-phase heterogeneity; (ii) the 2.25 μm band provides the dominant incremental constraint on FRP; and (iii) the VIIRS DNB is pivotal for stabilizing temperature partitioning and thus Q^f_{conv}. At night, the added shortwave/visible information (DNB, 1.6 μm) enables high-accuracy retrievals even with moderate heterogeneity. By contrast, for daytime observations, smoldering-dominated cases should be screened before relying on heat-flux–related quantities.

5. Concluding Remarks

This paper provides the theoretical basis for a two-part study aimed at advancing sub-pixel fire characterization using multi-channel satellite observations. We present a rigorous evaluation of sub-pixel fire characterization through a series of Observing System Simulation Experiments (OSSEs), using a Bayesian inference framework for retrieving fire properties. By systematically isolating the effects of model complexity, observation channel configuration, and intra-phase temperature heterogeneity, we provide new insights into the capabilities and limitations of current remote sensing systems for retrieving fire radiative properties at sub-pixel scales. In part II (Zhou et al., 2026), we apply this algorithm to actual satellite data.

Our results show that while a mono-phasic fire model may achieve reasonable estimates of total fire radiative power (FRP), it fails to capture the spectral nuances associated with heterogeneous fire conditions, leading to significant errors in derived parameters such as visible energy fraction (VEF) and flaming heat fluxes, quantities that are critical for modulating emission coefficients and plume injection heights. The bi-phasic model offers a strong balance between performance and observational feasibility, achieving robust accuracy across a range of configurations and proving resilient to moderate temperature heterogeneity. Although tri-phasic models exhibit marginal performance gains, their increased parameter space are more difficult to constrain given the limited spectral bands in current satellite systems.

We further demonstrate that certain shortwave and midwave infrared channels, particularly the visible DNB and 2.25 μm bands, are essential for constraining key fire parameters. Their combination enables improved estimation of phase-resolved temperatures and heat fluxes. However, we also show that intra-phase temperature heterogeneity introduces systematic biases, which vary across band configurations. These effects are especially pronounced when shorter-wavelength constraints are absent. In such cases, simple filtering techniques based on band ratios (e.g., R_{nir}) may help flag low-confidence retrievals, particularly in smoldering-dominated fires.

In terms of retrieval performance, FRP derived from the Markov-Chain Monte Carlo (MCMC) Bayesian algorithm showed significantly higher accuracy compared to the conventional Wooster regression approach, particularly in low-FRP regimes where the latter tended to severely underestimate FRP. Among all evaluated fire properties, FRP was the most resilient to reductions in channel availability and to intra-phase temperature heterogeneity. By contrast, flaming heat fluxes (Q_f^{rad} and Q_f^{conv}) were more sensitive to changes in model assumptions and observational constraints, reflecting their stronger dependence on accurate temperature partitioning. These results highlight the importance of both channel selection and model complexity when the goal is to characterize not only total fire energy but also combustion phase dynamics.

Taken together, these findings support the use of a bi-phasic model with carefully selected channels—such as those available on VIIRS for operational sub-pixel fire characterization. They also underscore the importance of future sensor development that includes well-calibrated shortwave channels to better constrain phase-specific fire behavior. The methodology and evaluation framework established here provide a solid foundation for both algorithm development and observation system design, contributing to improved understanding of wildfire energetics and atmospheric impacts.

To maintain controlled conditions, we assume idealized observations derived from known synthetic fire scenes, with simplified atmospheric and surface effects. While these assumptions enable a systematic analysis, they do not capture the full complexity of real-world remote sensing, including cloud cover, surface heterogeneity, view angle effects, and sensor calibration issues. Additionally, while we evaluate multiple parametric models (mono-, bi-, and tri-phasic), the dynamic selection of model structure and uncertainty handling are beyond the scope of this study and are addressed in the companion paper, which applies the framework to real VIIRS nighttime observations. In the companion paper, we apply the bi-phasic multi-channel Bayesian estimation framework to actual VIIRS nighttime observations and evaluate its performance using actual fire events.

6. Data available statement

The VIIRS sensor response function are obtained from NOAA's Center for Satellite Applications and Research. (https://ncc.nesdis.noaa.gov/VIIRS/VIIRSSpectralResponseFunctions.php). The McBEF software is available at Goddard Earth Observing System-Earth System Modeling (https://github.com/GEOS-ESM/FILDA/tree/main/src/MCBEF).

7. CRediT authorship contribution statement

Meng Zhou: Writing - review&editing, Writing-original draft, Visualization, Validation, Software, Resources, Project administration, Methodology, Investigation, Formal analysis, Data curation, Conceptualization. Arlindo M. da Silva:Writing-review&editing, Methodology, Investigation, Formal analysis, Conceptualization, Funding acquisition. Jun Wang: Writing-review&editing, Software, Resources, Funding acquisition. David A. Peterson: Writing - review&editing, Formal analysis, Resources.

8. Acknowledgment

This work has been supported by NASA's MAP and MEaSURES programs. The authors thank NOAA's Center for Satellite Applications and Research (NOAA STAR) for maintenance of VIIRS sensor response function. Special thanks are expressed to Gonzalo Ferrada (CIRES/NOAA) for the insight discussion across different stages of the McBEF development. As a response to the changing climate of open-source development, we gratefully acknowledge the PyMC developers and community for the PyMC probabilistic-programming framework, which we used for MCMC sampling (NUTS and Metropolis) in McBEF (Salvatier et al., 2016; Abril-Pla et al., 2023).

Appendix A. Supplementary materials

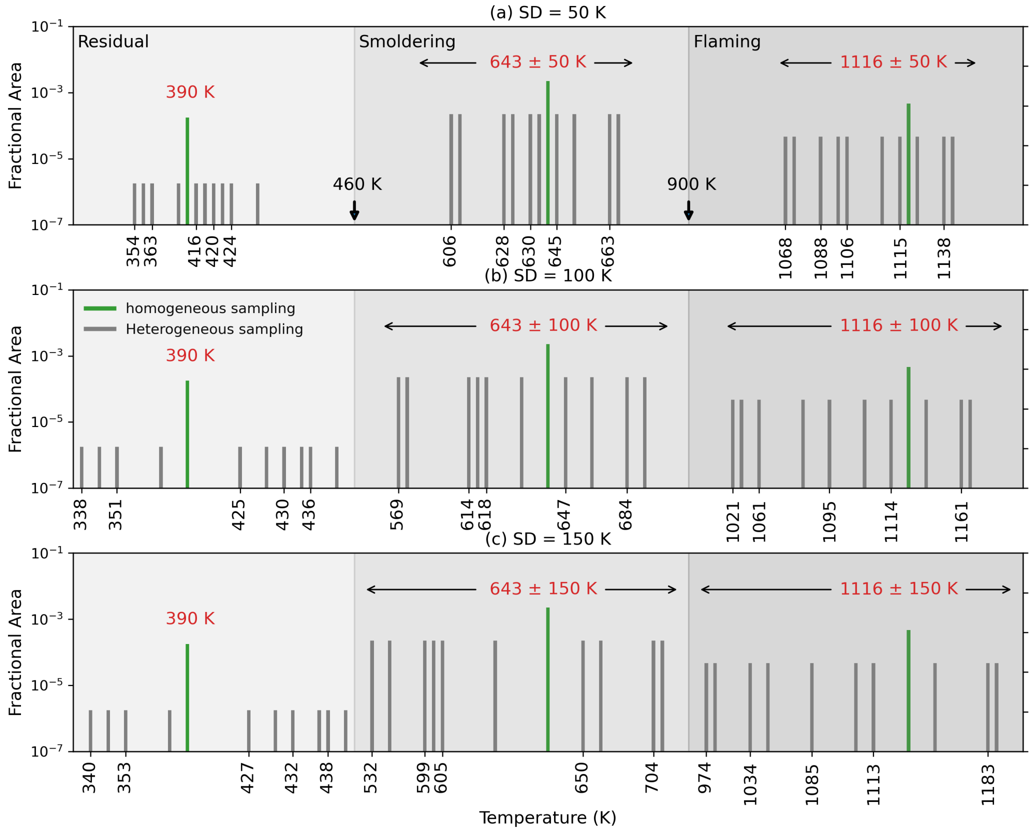

Figure A.12: Examples of temperature sampling for the nature run.

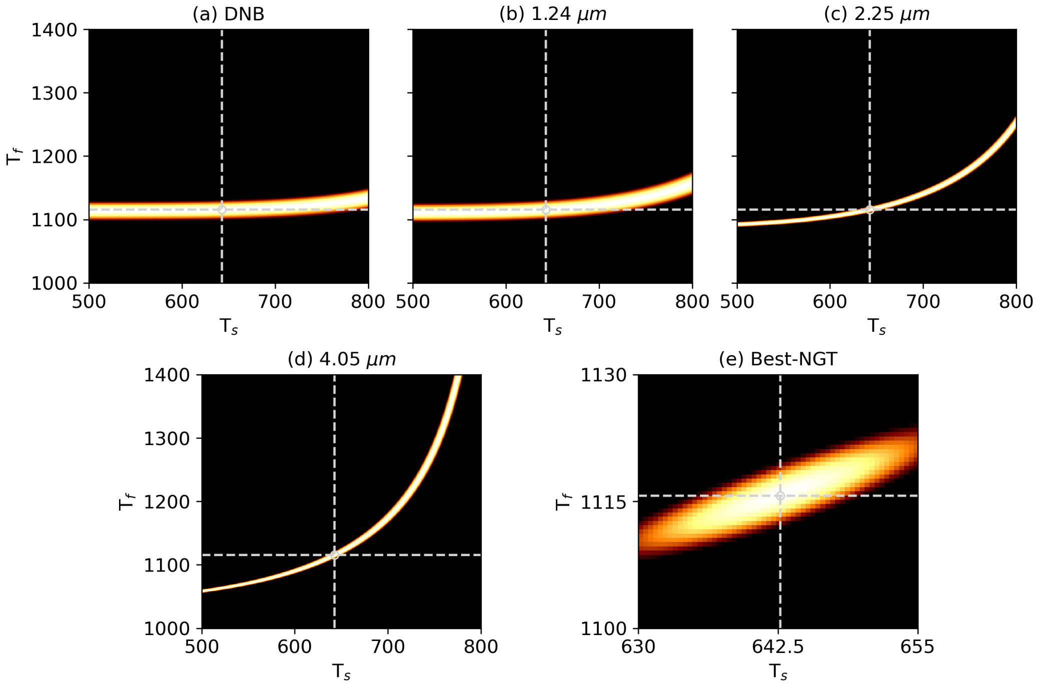

Figure A.13: The likelihood of (a) DNB, (b) 1.24 μm, (c) 1.60 μm, (d) 2.25 μm, and the joint-likelihood for the band configuration of Best-NGT (DNB, 1.24 μm, 1.60 μm, 2.25 μm, 4.05 μm, 8.55 μm, 10.5 μm, and 12.01 μm). Observations from 1.6 and 12.01 μm are used to solve the p_s and p_f for the given combination of T_s and T_f following the standard BSDM approach.

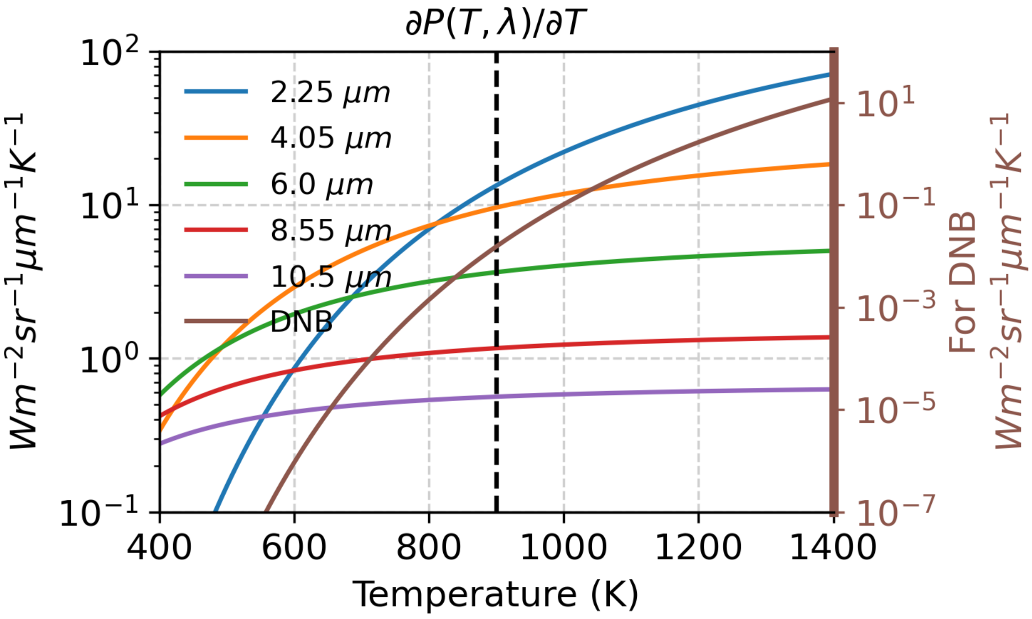

Figure A.14: Partial derivative of the Plank's function toward temperature for selectd bands.

Appendix A.1. Further discussion on the error distributions full-scenario evaluation for Impact of Intra-phase Temperature Heterogeneity

Fig. A.15 summarizes the full-scenario evaluation for impact of intra-phase temperature heterogeneity. Consistent with earlier findings, FRP shows the strongest resilience to both intra-phase temperature variation and reductions in the number of observation bands. Across all enhanced band configurations (i.e., those with additional channels beyond the threshold), FRP relative errors remain within 2%. Although an uptick in error is observed with increasing temperature variation, particularly for USS, BEST-NGT, and VIIRS-NGT, the maximum increase is only about 0.5%, indicating relatively minor sensitivity. Notably, much of the improvement over the threshold can be attributed to the inclusion of the 2.25 μm band. This is evident when comparing BEST-NGT or VIIRS-NGT with VIIRS-Day: despite the former configurations including additional shorter bands (DNB, 1.24 μm , 1.6 μm), FRP estimation accuracy does not improve significantly beyond what is achieved with VIIRS-Day, which only includes 2.25 μm.

The USS, BEST-NGT, and VIIRS-NGT configurations also demonstrate strong performance in reconstructing $\ln(\mathcal{V})$, with relative errors below 2%. Not surprisingly, omitting shortwave observations significantly increases error. For instance, the SLSTR-NGT configuration, lacking DNB and 1.24 μm, shows errors exceeding 10%, and VIIRS-Day reaches up to 20% error, with only 2.25 μm as the shortwave constraint. The effect of intra-phase temperature variation is twofold: it increases the overall relative error and introduces systematic biases that vary with band configuration. For example, USS exhibits a consistent negative bias as variation increases, BEST-NGT shows a reduced bias, and VIIRS-NGT even shows a positive bias. These trends are primarily due to differences in band sensitivity to temperature and their respective abilities to constrain the estimation. Further explanation is provided in the supplementary materials (Figs. A.17 and A.16). While VIIRS-Day can have up to 20% error in $\ln(\mathcal{V})$, estimates of MCE from VEF is less affected. Recall that $MCE \approx 1 + 0.017 \ln(\mathcal{V})$ (see Wang et al., 2020a; Zhou et al., 2023). Given that $\ln(\mathcal{V})$ typically ranges from -12 to -3, the resulting propagated MCE error remains within 0.004, or less than 0.4%.

The radiative and convective heat fluxes, Q^f_{rad} and Q^f_{conv}, are the most sensitive to both temperature variation and channel selection. This is expected, as these derived properties rely on the partitioning of radiance across temperature phases rather than the total radiance alone, thus less directly

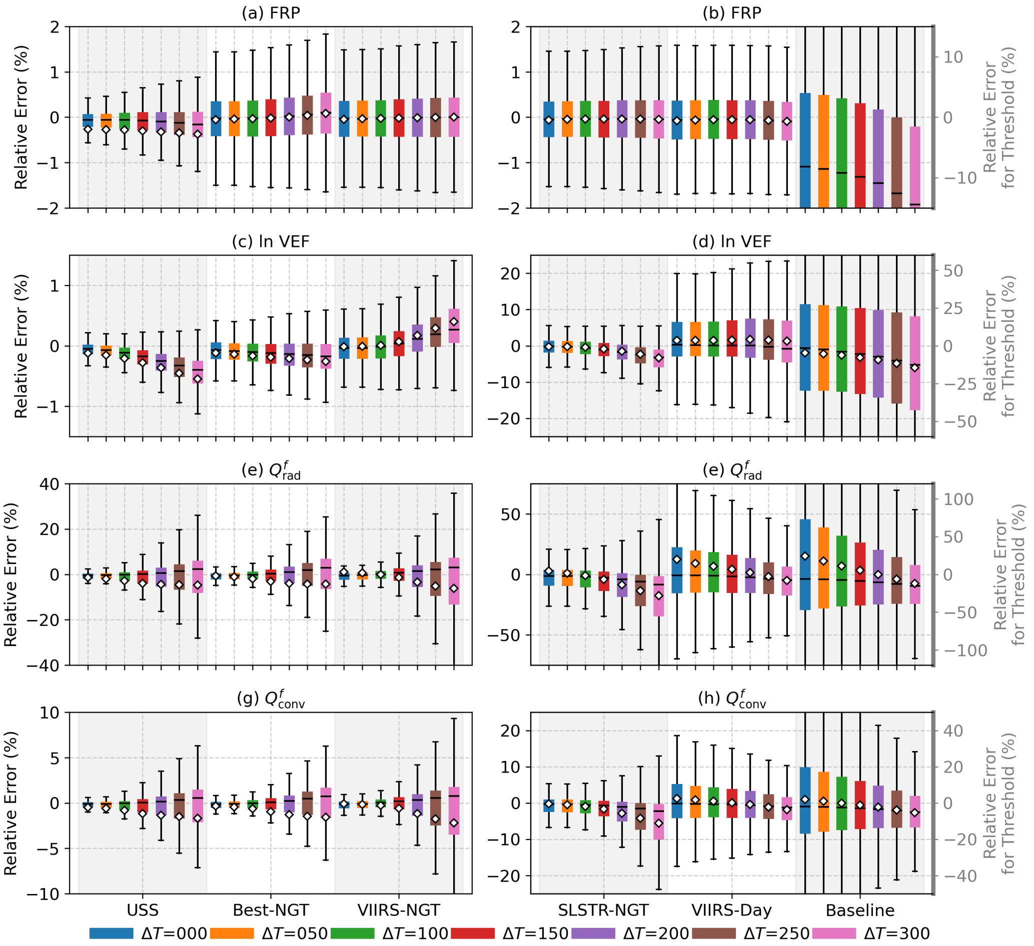

Figure A.15: Statistic summary of the evaluation of OSSEs using the proposed four metrics for investigating impact intra-phase temperature heterogeneity. Seven levels of temperature variation are investigated and are denoted as blue for 0 K, orange for 50 K, green for 100 K, red for 150 K, purple for 200 K, brown for 250 K, and pink for 300 K. Six band configurations are considered. The error range for the threshold band configuration are shown left Y-axis of (b), (d), (f), and (h).

constrained by data. While the total spectral shape may be well estimated, insufficient constraint can lead to poor partitioning. Additionally, the relative errors in Q^f_{rad} and Q^f_{conv} are modulated by the defined sampling range for flaming temperatures. Based on these ranges, the allowable minimum-maximum relative error for each temperature variation range can be computed (Table A.5). Not surprisingly, Q^f_{rad} exhibits a wider error range than Q^f_{conv}, as it scales with T^4, amplifying temperature-related uncertainties. Using these bounds, Fig. A.15 shows that BEST-NGT and VIIRS-NGT not only have small relative errors for Q^f_{rad} and Q^f_{conv} but also utilize only a small portion of their respective error ranges. For instance, relative errors in Q^f_{conv} are generally below 10%, while the allowed maximum error is around 50%, meaning only 20% of the full error space is used. This aligns with results from Section 4.3, where DNB was shown to provide the strongest constraint on flaming temperature, and longer wavelengths were less effective.

Table A.5: Allowed minimum-maximum relative error of Q^f_{rad} and Q^f_{conv}

σ_{Tf}	$\overline{T_f}$ sampling range	Q^f_{rad}	Q^f_{conv}
0	$U(900, 1400)$	(-82.92%, 485.52%)	(-35.71%, 55.56%)
50	$U(925, 1375)$	(-81.64%, 424.74%)	(-34.55%, 51.35%)
100	$U(950, 1350)$	(-80.25%, 371.65%)	(-33.33%, 47.37%)
150	$U(975, 1325)$	(-78.71%, 325.10%)	(-32.08%, 43.59%)
200	$U(1000, 1300)$	(-77.03%, 284.16%)	(-30.77%, 40.00%)
250	$U(1025, 1275)$	(-75.17%, 248.03%)	(-29.41%, 36.59%)
300	$U(1050, 1250)$	(-73.13%, 216.05%)	(-28.00%, 33.33%)

Appendix A.2. Further discussion on the sensitivity of VEF to fire heterogeneity.

Together, Fig. A.16 and Fig. A.17 provide a physical explanation for the $\ln(\mathcal{V})$ trends observed in Fig. A.15. These patterns result from error propagation across parameters in the retrieval process. Specifically, the sensitivity of spectral radiance to intra-phase temperature heterogeneity is coupled with both the central temperature and wavelength. While the relationships are complex, Fig. A.16 indicates that visible (VIS), near-infrared (NIR), and mid-wave infrared (MWIR) bands are generally more sensitive to temperature heterogeneity than thermal infrared (TIR) bands.

For instance, at a central temperature of 500 K, a 150 K variation increases radiance at 2.25 μm by roughly three times more than at 8 μm. As the central temperature increases, the peak of radiance sensitivity also shifts toward shorter wavelengths. This observation aligns with Fig. A.14, which shows that the derivative of Planckian radiance with respect to temperature flattens at longer wavelengths (beyond 8 μm), indicating low temperature sensitivity in the TIR region.

Fig. A.14 also shows that smoldering temperatures contribute little to the VIS and NIR radiance compared to the flaming phase. In the USS configuration, 40 out of 115 channels fall in the 8∼12 μm range. This heavy weighting toward the TIR region leads to underestimation of smoldering contributions at shorter wavelengths (e.g., 2∼4 μm), as illustrated in Fig. A.17. These underestimations propagate through the fitting process and lead to compensatory overestimation of the flaming component.

At the same time, temperature variation within the flaming phase causes an upward bias in T_f as the retrieval attempts to capture spectral variation in the VIS and NIR regions, an effect also seen in Fig. 11, particularly after filtering out smoldering-dominated cases in Q^f_{conv}. Consequently, overestimation of T_f is driven by both misfitting in the VIS/NIR and error compensation for the smoldering phase.

However, an overestimated T_f also leads to excessive flaming radiance in the TIR bands. To reduce this mismatch, the algorithm tends to underestimate p_f, which reduces the total TIR flaming radiance. This reduction, in turn, lowers the visible band contribution from the flaming phase, leading to a net underestimation of $\ln(\mathcal{V})$.

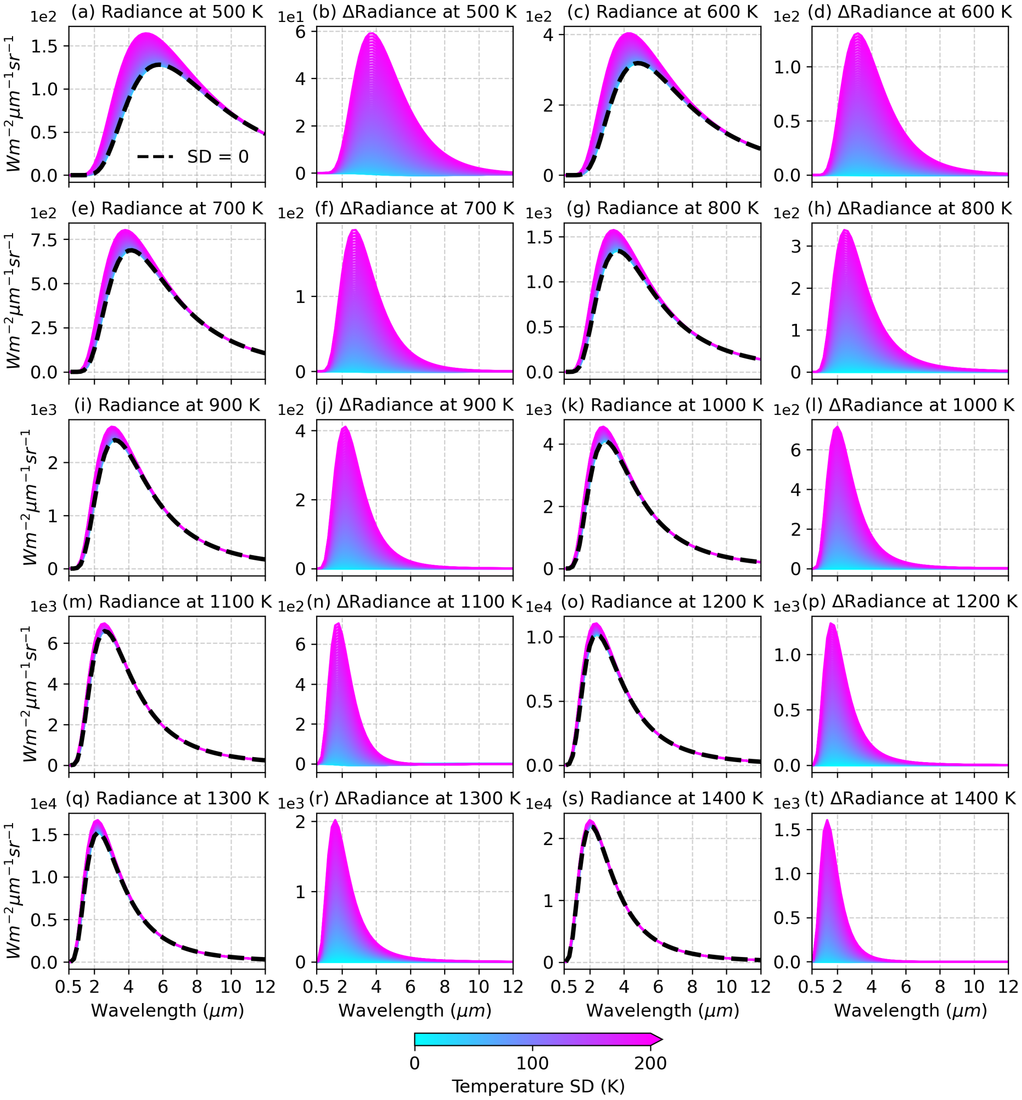

Figure A.16: Spectral radiance and the corresponding radiance increment as a function of temperature variations for selected the temperature.

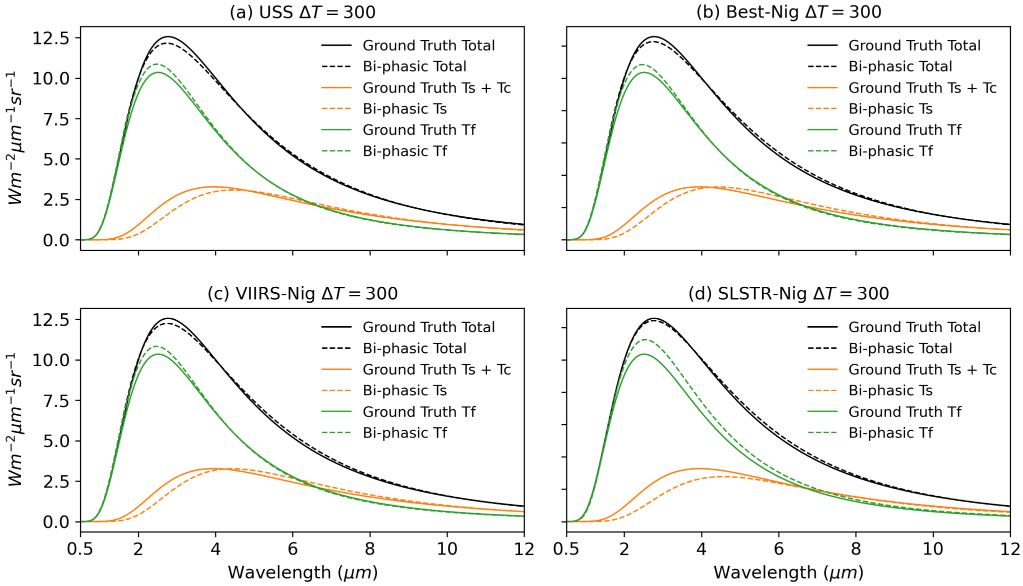

Figure A.17: Reconstructed spectral radiance of the selected band configurations for the temperature heterogeneity of 300 K.

References

John T Abatzoglou and A Park Williams. Impact of anthropogenic climate change on wildfire across western us forests. *Proceedings of the National Academy of Sciences*, 113(42):11770–11775, 2016.

Oriol Abril-Pla, Virgile Andreani, Colin Carroll, Larry Dong, Christopher J Fonnesbeck, Maxim Kochurov, Ravin Kumar, Junpeng Lao, Christian C Luhmann, Osvaldo A Martin, et al. Pymc: a modern, and comprehensive probabilistic programming framework in python. *PeerJ Computer Science*, 9:e1516, 2023.

ASTM. 2000 astm standard extraterrestrial spectrum reference e-490-00. Technical report, the American Society for Testing and Materials, 2000. URL https://www.nrel.gov/grid/solar-resource/spectra-astm-e490.html.

Michael Betancourt. A conceptual introduction to hamiltonian monte carlo. *arXiv preprint arXiv:1701.02434*, 2017.

VG Bondur, II Mokhov, OS Voronova, and SA Sitnov. Satellite monitoring of siberian wildfires and their effects: Features of 2019 anomalies and trends of 20-year changes. In *Doklady Earth Sciences*, volume 492, pages 370–375. Springer, 2020.

Changyong Cao, Frank J De Luccia, Xiaoxiong Xiong, Robert Wolfe, and Fuzhong Weng. Early on-orbit performance of the visible infrared imaging radiometer suite onboard the suomi national polar-orbiting partnership (s-npp) satellite. *IEEE Transactions on Geoscience and Remote Sensing*, 52 (2):1142–1156, 2013.

Emilio Chuvieco, Inmaculada Aguado, Javier Salas, Mariano García, Marta Yebra, and Patricia Oliva. Satellite remote sensing contributions to wildland fire science and management. *Current Forestry Reports*, 6:81–96, 2020.

CBO Congressional Budget Office. Wildfires. Technical report, Congressional Budget Office, June 2022. URL https://www.cbo.gov/publication/57970. Accessed: 2025-03-28.

Ivan Csiszar, Wilfrid Schroeder, Louis Giglio, Evan Ellicott, Krishna P Vadrevu, Christopher O Justice, and Brad Wind. Active fires from the suomi npp visible infrared imaging radiometer suite: Product status and first evaluation results. *Journal of Geophysical Research: Atmospheres*, 119(2):803–816, 2014.

A. Darmenov and A. M. da Silva. The Quick Fire Emissions Dataset (QFED): Documentation of versions 2.1, 2.2 and 2.4. *Technical Report Series on Global Modeling and Data Assimilation*, 38:1 – 212, 09 2015. URL https://gmao.gsfc.nasa.gov/pubs/docs/Darmenov796.pdf.

Diane K Davies, Shriram Ilavajhala, Min Minnie Wong, and Christopher O Justice. Fire information for resource management system: archiving and distributing modis active fire data. *IEEE Transactions on Geoscience and Remote Sensing*, 47(1):72–79, 2008.

Weizhi Deng, Meng Zhou, Jun Wang, Zhixin Xue, Zhendong Lu, Xi Chen, Huanxin Zhang, David A Peterson, Edward J Hyer, and Arlindo M Da Silva. Advancing frp retrieval: Bridging theory and application. *IEEE Transactions on Geoscience and Remote Sensing*, 2024.

Jeff Dozier. A method for satellite identification of surface temperature fields of subpixel resolution. *Remote Sensing of environment*, 11:221–229, 1981.

TC Eckmann, DA Roberts, and CJ Still. Estimating subpixel fire sizes and temperatures from aster using multiple endmember spectral mixture analysis. *International Journal of Remote Sensing*, 30(22):5851–5864, 2009.

Saulo R Freitas, Karla M Longo, Robert Chatfield, D Latham, Maria Assunção Faus da Silva Dias, MO Andreae, E Prins, JC Santos, R Gielow, and JA Carvalho Jr. Including the sub-grid scale plume rise of vegetation fires in low resolution atmospheric transport models. *Atmospheric Chemistry and Physics*, 7(13):3385–3398, 2007.

Andrew Gelman, John B Carlin, Hal S Stern, and Donald B Rubin. *Bayesian data analysis*. Chapman and Hall/CRC, 1995.

Louis Giglio and Jacqueline D Kendall. Application of the dozier retrieval to wildfire characterization: A sensitivity analysis. *Remote sensing of Environment*, 77(1):34–49, 2001.

Louis Giglio, GR Van der Werf, JT Randerson, GJ Collatz, and Pedro Kasibhatla. Global estimation of burned area using modis active fire observations. *Atmospheric Chemistry and Physics*, 6(4):957–974, 2006.

Louis Giglio, Wilfrid Schroeder, and Christopher O Justice. The collection 6 modis active fire detection algorithm and fire products. *Remote sensing of environment*, 178:31–41, 2016.

Michael Goss, Daniel L Swain, John T Abatzoglou, Ali Sarhadi, Crystal A Kolden, A Park Williams, and Noah S Diffenbaugh. Climate change is increasing the likelihood of extreme autumn wildfire conditions across california. *Environmental Research Letters*, 15(9):094016, 2020.

Matthew D Hoffman, Andrew Gelman, et al. The no-u-turn sampler: adaptively setting path lengths in hamiltonian monte carlo. *J. Mach. Learn. Res.*, 15(1):1593–1623, 2014.

CO Justice, Louis Giglio, S Korontzi, J Owens, JT Morisette, D Roy, J Descloitres, S Alleaume, F Petitcolin, and Y Kaufman. The modis fire products. *Remote sensing of Environment*, 83(1-2):244–262, 2002.

J. Kaiser, A. Heil, M.G. Schultz, S. Remy, O. Stein, G. van der Werf, M. Wooster, and W. Xu. Final report on implementation and quality of the d-fire assimilation system, 07/2013 2013. URL https://www.ecmwf.int/node/10360.

Yoram J Kaufman, Christopher O Justice, Luke P Flynn, Jackie D Kendall, Elaine M Prins, Louis Giglio, Darold E Ward, W Paul Menzel, and Alberto W Setzer. Potential global fire monitoring from eos-modis. *Journal of Geophysical Research: Atmospheres*, 103(D24):32215–32238, 1998.

Raymond F Kokaly, Roger N Clark, Gregg A Swayze, K Eric Livo, Todd M Hoefen, Neil C Pearson, Richard A Wise, William Benzel, Heather A Lowers, Rhonda L Driscoll, et al. Usgs spectral library version 7. Technical report, US Geological Survey, 2017.

Fangjun Li, Xiaoyang Zhang, Shobha Kondragunta, Xiaoman Lu, Ivan Csiszar, and Christopher C Schmidt. Hourly biomass burning emissions product from blended geostationary and polar-orbiting satellites for air quality forecasting applications. *Remote Sensing of Environment*, 281: 113237, 2022.

Zhangqing Li, Yoram J Kaufman, Charles Ichoku, Robert Fraser, Alex Trishchenko, Louis Giglio, J Jin, and Xinwen Yu. A review of avhrr-based active fire detection algorithms: Principles, limitations, and recommendations. *Global and regional vegetation fire monitoring from space, planning and coordinated international effort*, pages 199–225, 2001.

W Timothy Liu, Kristina B Katsaros, and Joost A Businger. Bulk parameterization of air-sea exchanges of heat and water vapor including the molecular constraints at the interface. *Journal of Atmospheric sciences*, 36(9):1722–1735, 1979.

WP Menzel, EC Cutrim, and EM Prins. Geostationary satellite estimation of biomass burning in amazonia during base-a, global biomass burning (js levine, ed), 1991.

Peter M Norris and Arlindo M da Silva. Monte carlo bayesian inference on a statistical model of sub-gridcolumn moisture variability using high-resolution cloud observations. part 2: Sensitivity tests and results. *Quarterly Journal of the Royal Meteorological Society*, 142(699):2528–2540, 2016.

Peter M Norris and Arlindo M da Silva. Monte Carlo Bayesian inference on a statistical model of sub-gridcolumn moisture variability using high-resolution cloud observations. Part 1: Method. *Quarterly Journal of the Royal Meteorological Society*, 142(699):2505 – 2527, 07 2016. doi: 10.1002/qj.2843.

Xiaohua Pan, Charles Ichoku, Mian Chin, Huisheng Bian, Anton Darmenov, Peter Colarco, Luke Ellison, Tom Kucsera, Arlindo da Silva, Jun Wang, et al. Six global biomass burning emission datasets: intercomparison and application in one global aerosol model. *Atmospheric Chemistry and Physics*, 20(2):969–994, 2020.

David Peterson and Jun Wang. A sub-pixel-based calculation of fire radiative power from modis observations: 2. sensitivity analysis and potential fire weather application. *Remote Sensing of Environment*, 129:231–249, 2013.

David Peterson, Jun Wang, Charles Ichoku, Edward Hyer, and Vincent Ambrosia. A sub-pixel-based calculation of fire radiative power from modis observations: 1: Algorithm development and initial assessment. *Remote Sensing of Environment*, 129:262–279, 2013.

David Peterson, Edward Hyer, and Jun Wang. Quantifying the potential for high-altitude smoke injection in the north american boreal forest using the standard modis fire products and subpixel-based methods. *Journal of Geophysical Research: Atmospheres*, 119(6):3401–3419, 2014.

Thomas N Polivka, Jun Wang, Luke T Ellison, Edward J Hyer, and Charles M Ichoku. Improving nocturnal fire detection with the viirs day–night band. *IEEE Transactions on Geoscience and Remote Sensing*, 54 (9):5503–5519, 2016.

Derek J Posselt. Markov chain monte carlo methods: Theory and applications. In *Data Assimilation for Atmospheric, Oceanic and Hydrologic Applications (Vol. II)*, pages 59–87. Springer, 2013.

Guillermo Rein. Smoldering combustion. *SFPE handbook of fire protection engineering*, pages 581–603, 2016.

Christian Robert and George Casella. A short history of markov chain monte carlo: Subjective recollections from incomplete data. 2011.

Clive D. Rodgers. Characterization and error analysis of profiles retrieved from remote sounding measurements. *Journal of Geophysical Research: Atmospheres*, 95(D5):5587–5595, 1990. ISSN 0148-0227. doi: 10.1029/jd095id05p05587.

Laurence S Rothman, Iouli E Gordon, Yury Babikov, Alain Barbe, D Chris Benner, Peter F Bernath, Manfred Birk, Luca Bizzocchi, Vincent Boudon, Linda R Brown, et al. The hitran2012 molecular spectroscopic database. *Journal of Quantitative Spectroscopy and Radiative Transfer*, 130:4–50, 2013.

John Salvatier, Thomas V Wiecki, and Christopher Fonnesbeck. Probabilistic programming in python using pymc3. *PeerJ Computer Science*, 2:e55, 2016.

Chris Schmidt. Monitoring fires with the goes-r series. In *The GOES-R Series*, pages 145–163. Elsevier, 2020.

Wilfrid Schroeder, Patricia Oliva, Louis Giglio, and Ivan A Csiszar. The new viirs 375 m active fire detection data product: Algorithm description and initial assessment. *Remote Sensing of Environment*, 143:85–96, 2014.

Danielle Touma, Samantha Stevenson, Daniel L Swain, Deepti Singh, Dmitri A Kalashnikov, and Xingying Huang. Climate change increases risk of extreme rainfall following wildfire in the western united states. *Science advances*, 8(13):eabm0320, 2022.

Guido R Van Der Werf, James T Randerson, Louis Giglio, Thijs T Van Leeuwen, Yang Chen, Brendan M Rogers, Mingquan Mu, Margreet JE Van Marle, Douglas C Morton, G James Collatz, et al. Global fire emissions estimates during 1997–2016. *Earth System Science Data*, 9(2):697–720, 2017.

Jun Wang, Sepehr Roudini, Edward J Hyer, Xiaoguang Xu, Meng Zhou, Lorena Castro Garcia, Jeffrey S Reid, David A Peterson, and Arlindo M Da Silva. Detecting nighttime fire combustion phase by hybrid application of visible and infrared radiation from suomi npp viirs. *Remote sensing of environment*, 237:111466, 2020a.

Jun Wang, Meng Zhou, Xiaoguang Xu, Sepehr Roudini, Stanley P Sander, Thomas J Pongetti, Steven D Miller, Jeffrey S Reid, Edward Hyer, and Robert Spurr. Development of a nighttime shortwave radiative transfer model for remote sensing of nocturnal aerosols and fires from viirs. *Remote sensing of environment*, 241:111727, 2020b.

D Ward. Combustion chemistry and smoke. In *Forest fires*, pages 55–77. Elsevier, 2001.

Carsten Warneke, Joshua P Schwarz, Jack Dibb, Olga Kalashnikova, Gregory Frost, Jassim Al-Saad, Steven S Brown, Wm Alan Brewer, Amber Soja, Felix C Seidel, et al. Fire influence on regional to global environments and air quality (firex-aq). *Journal of Geophysical Research: Atmospheres*, 128 (2):e2022JD037758, 2023.

Martin J Wooster, Weidong Xu, and T Nightingale. Sentinel-3 slstr active fire detection and frp product: Pre-launch algorithm development and performance evaluation using modis and aster datasets. *Remote sensing of environment*, 120:236–254, 2012.

MJ Wooster, B Zhukov, and D Oertel. Fire radiative energy for quantitative study of biomass burning: Derivation from the bird experimental satellite and comparison to modis fire products. *Remote Sensing of Environment*, 86(1):83–107, 2003.

Rongbin Xu, Pei Yu, Michael J Abramson, Fay H Johnston, Jonathan M Samet, Michelle L Bell, Andy Haines, Kristie L Ebi, Shanshan Li, and Yuming Guo. Wildfires, global climate change, and human health. *New England Journal of Medicine*, 383(22):2173–2181, 2020.

Meng Zhou, Jun Wang, Lorena Castro Garcia, Xi Chen, Arlindo M da Silva, Zhuosen Wang, Miguel O Román, Edward J Hyer, and Steven D Miller. Enhancement of nighttime fire detection and combustion efficiency characterization using suomi-npp and noaa-20 viirs instruments. *IEEE Transactions on Geoscience and Remote Sensing*, 61:1–20, 2023.

Meng Zhou, Arlindo M. da Silva, Jun Wang, and David A. Peterson. Montecarlo biphasic estimation of fire properties (mcbef): Part ii, night-time viirs implementation. *Remote Sensing of Environment*, 2026. submitted.

Ciyou Zhu, Richard H Byrd, Peihuang Lu, and Jorge Nocedal. Algorithm 778: L-bfgs-b: Fortran subroutines for large-scale bound-constrained optimization. *ACM Transactions on mathematical software (TOMS)*, 23(4): 550–560, 1997.